Searches for new neutral and charged scalars with multiple top and bottom quarks in Run 2 pp collisions at $\sqrt{s} = 13$ TeV with the ATLAS detector

Customise this page according to your needs

Adrian Salvador Salas

July 25, 2022

An Awesome Publisher

Somewhere, something incredible is waiting to be known.

– Carl Sagan

Abstract

This thesis presents two searches for new scalars produced with the 139 fb$^{-}1$ proton-proton collision data at a centre-of-mass energy of 13 TeV, collected by the ATLAS detector at the CERN Large Hadron collider during Run 2. Both searches are performed in multi-jet final states with one electron or muon and events categorised according to the multiplicity of jets and how likely these are to have originated from the hadronisation of a bottom quark. Parameterised feed-forward neural networks are used to discriminate between signal and background and included in maximum-likelihood fits to the data for the different mass hypotheses.

The first search is dedicated to charged Higgs bosons, predicted by various theories Beyond the Standard Model and motivated by the inadequacy of the Standard Model to explain some experimental phenomena. The work focuses on heavy charged Higgs bosons, heavier than the top quark, and decaying to a pair of top and bottom quarks, $H^{\pm} \rightarrow tb$, while the production is in association with a top and a bottom quark, $pp \rightarrow tbH^{\pm}$. The search is performed in the mass range between 200 and 2000 GeV. No significant excess of events above the expected Standard Model background is observed, hence upper limits are set for the cross-section of the charged Higgs boson production times the branching fraction of its decay. Results are interpreted in the context of hMSSM, various Mh125 scenarios and 2HDM+a.

The second search targets FCNC decays of top quarks into a new scalar decaying into a pair of bottom quarks, $t \rightarrow u/cX(bb)$, in $t\bar{t}$ events. This novel study probes for the scalar on a broad mass range between 20 and 160 GeV and branching ratios below 10^{-3}. In the case of the Higgs boson, branching ratios for $t \rightarrow u/cH$ are predicted within the Standard Model to be of $\mathcal{O}(10^{-17})/\mathcal{O}(10^{-15})$. Several Beyond the Standard Model theoretical models predict new particles and enhanced branching ratios. In particular, simple extensions involve the Froggatt-Nielsen mechanism, which introduces a scalar field with flavour charge, the so-called flavon, featuring flavour violating interactions. As no significant excess is observed, upper limits for both FCNC decays $t \rightarrow uX$ and $t \rightarrow cX$ are computed. In addition, limits are set for the process involving the Standard Model Higgs.

Contents

Introduction

The discovery of the Higgs boson in 2012 by ATLAS and CMS [1, 2] is one of the most recent historic milestones in the field of particle physics. CERN hosts the LHC, which physics' program included the hunt of the Higgs boson. After this achievement, all particles predicted by the Standard Model are discovered, the theory which describes the fundamental particles and their interactions. Nevertheless, the ATLAS experiment continues to scrutinise the Standard Model of particle physics by analysing the ever-increasing amount of particle collisions delivered by the LHC. There are many phenomena not covered by the current theory and any measurement that deviates from the predictions or any hint of a new particle will lay the foundation for a new path in particle physics.

The theory of the Standard Model has successfully guided the experiments with the prediction of particles and precise values of their interactions. However, no other theory has been able to explain the tiny deviations with respect to the theory or filled the gaps that the Standard Model does not even contemplate. Known tensions with respect to the theory predictions are regarding the lepton universality [3] or the measurement of the anomalous magnetic dipole momentum of the muon (g-2) [4]. On the other hand, the theory fails to cover gravity, the neutrino masses, dark matter... although one of the most compelling concerns regarding the Standard Model is known as the hierarchy problem, the seemingly unnatural fact that the Higgs mass, yet not having any constrain in the theory, appears to be at the electroweak scale. One of the possible theoretical solutions consinsts in an expansion of the Standard Model which spawns additional scalar particles. If the Higgs sector is built with one extra doublet (Two Higgs Doublet Models), a total of five scalars are predicted instead, including Higgs bosons with electrical charge. Another similar feature of the Standard Model is known as the flavour problem, as fermions can be grouped in three families with different mixing patterns, which is also seen as arbitrary choice. This feature can be explained by introducing a broken flavour symmetry spawning a new particle, the flavon, which introduced flavour violating interactions. The presence of flavour-changing neutral current (FCNC) interactions is heavily suppressed in the Standard Model, way below the available sensitivity. These interactions are hence very sensitive to new physics as any observed interaction cannot be explained by the Standard Model.

In this thesis, a direct search for charged Higgs bosons heavier than the top quark and a direct search for neutral scalars lighter than the top quark are presented. The charged Higgs process is searched in the $200 - 2000$ GeV mass range produced in association with top and bottom quarks and decaying into a top-bottom, while the neutral scalar is searched in the $20 - 160$ GeV mass range produced in the FCNC decay of a top quark involving a c- or a u-quark, and finally decaying to a pair of b-quarks. Limits on the production of charged Higgs bosons in the same channel have been previously obtained by ATLAS with only the data from 2015 and 2016 for $H^{\pm} \to tb$ in the $200 - 2000$ GeV mass range [5], and more recently by CMS in the

$200 - 3000 TeV$ GeV mass range using the full Run-2, setting upper limits at 95% confidence level on the production cross section of 2.9 − 0.070 pb and 9.6 − 0.01 pb respectively. On the other hand, both ATLAS and CMS have searched for the top FCNC decay into the SM Higgs, $t \longrightarrow qH$ with q being either a c- or u-quark. Both ATLAS and CMS have performed multiple measurements on this process, the most recent from ATLAS being in the $H \longrightarrow \tau\tau$ channel [6] while the CMS results with 137 fb^{-1} data combines several channels and sets the limits to $t \longrightarrow uH < 0.079$ and $t \longrightarrow cH < 0.094$ [7]. However, these results are for the SM Higgs and the generic signature of a scalar lighter than the top quark presented in this work is uncovered in literature.

Both searches performed in this thesis are performed using the full Run-2 proton-proton collisions collected by the ATLAS experiment from 2015 to 2018 at a center-of-mass energy of 13 TeV. Events are selected to have either one electron or muon and multiple jets, including those originated from the hadronisation of a bottom quark. Results are extracted by means of binned maximum-likelihood fits of the different simulated signal and SM backgrounds to the recorded data. The fit is performed on a discriminant obtained by combining several kinematic variables through the training of parameterised feed-forward neural networks, developed to optimise the sensitivity by separating signal and background events.

The document is structured into three main parts: The first part describes the theoretical and experimental setup, while the second part includes the $H^{\pm} \longrightarrow tb$ analysis while the third part includes the $t \longrightarrow qX$ analysis, both with a detailed description of the strategy and their results. Chapter 1 focuses on the Standard Model and the models that motivate the searches. Chapter 2 provides an overview of the LHC and the ATLAS experiment. Chapters 3 and 4 present the essential aspects of the simulation and reconstruction of simulated proton-proton collisions, while Chapter 5 presents the machine learning techniques and statistical tools used in the different analyses.

tocomplete

Theoretical and experimental setup

The Standard Model of Particle Physics and beyond

1

The Standard Model (SM) of particle physics [8–10] is the theoretical framework that so far better describes subatomic particles and their interactions. It is a Quantum Field Theory (QFT) and since its initial development in the 1960's, the model has been overwhelmingly successful and guided many experimental achievements including the discovery of the top quark [11, 12] in 1995 and the Higgs boson at the LHC in 2012 [1, 2]. Regardless of its success, there are known phenomena not covered in the model and other questions which clearly point to the need of a new theories.

This chapter starts with an overview of the SM, building it with its mathematical formalism, and presenting a summary of the particle content and their interactions as of yet. Then, it continues with a summary of the current success of the theory, but also shortcomings and alternative models that could serve as solutions. The focus is given to models that include charged Higgs bosons or top FCNC interactions involving a scalar.

Throughout this dissertation, natural units are used: the speed of light and the reduced Plank constant are set to unity ($c = \hbar = 1$), electric charges are expressed in units of the electron electric charge ($-e$) and masses are expressed in terms of energy (eV). Within the theoretical developments in this chapter, the Einstein's summation convention is used by default.

1.1 The Standard Model of Particle Physics

From the mathematical point of view, the SM is a renormalisable non-abelian gauge QFT based on the symmetry group,

$$SU(3)_C \otimes SU(2)_L \otimes U(1)_Y \tag{1.1}$$

where $SU(3)_C$ is the group described by Quantum Chromodynamics (QCD) [13] that represents the strong interactions of colored quarks and gluons (strong force), while $SU(2)_L \times U(1)_Y$ is the inclusive representation of both electromagnetic (EM) and weak interactions described by the ElectroWeak (EW) theory [8, 9, 14]. The SM describes all the interactions between elementary particles except gravity, for which no renormalisable QFT has been formulated so far. The following sections, introduce the particles of the SM and the theories that describe their interactions.

1.1.1 Particle content of the Standard Model

In the SM, elementary particles are described as excitations of quantum fields. There are two main classes of particles within the theory: *fermions* and *bosons*. The main difference between the two is the spin: fermions have half-integer spin and therefore obey the Pauli exclusion principle [15], while bosons have integer spin.

Fermions

Fermions can be divided further into two categories: quarks and leptons, based on their interactions, or their charges. Both types manifest in EW interactions, having a weak isospin $T_3 = \pm 1/2$ while only the quarks experience the strong interaction. Quarks have a fractional electric charge $|Q| = 2/3$ or $1/3$, and the *colour*. The last one is the charge associated to the strong interaction and its values are denoted as *red*, *green* and *blue*. Table 1.1 presents a summary of the fundamental fermions and their characteristics.

Table 1.1: Table of the different quarks and leptons of the SM grouped in families with their mass and electric charge according to the Particle Data Group [16]. The uncertainties on the electron and the muon masses are below 10^{-10} and 10^{-6} MeV, respectively. The anti-matter states are not shown.

Generation	Name	Symbol	Mass	Charge
		Quarks		
1$^{\text{st}}$	Up	u	$2.15^{+0.49}_{-0.26}$ MeV	$+2/3$
	Down	d	$4.67^{+0.48}_{-0.17}$ MeV	$-1/3$
2$^{\text{nd}}$	Charm	c	1.27 ± 0.02 GeV	$+2/3$
	Strange	s	$93.4^{+8.6}_{-3.4}$ MeV	$-1/3$
3$^{\text{rd}}$	Top	t	172.69 ± 0.30 GeV	$+2/3$
	Bottom	b	$4.18^{+0.03}_{-0.02}$ GeV	$-1/3$
		Leptons		
1$^{\text{st}}$	Electron	e^-	0.511 MeV	-1
	Electron neutrino	ν_e	< 1.1 eV 90% CL	0
2$^{\text{nd}}$	Muon	μ^-	0.106 GeV	-1
	Muon neutrino	ν_μ	< 0.19 MeV 90% CL	0
3$^{\text{rd}}$	Tau	τ^-	1776.86 ± 0.12 MeV	-1
	Tau neutrino	ν_τ	< 18.2 MeV 95% CL	0

There is a total of six quark types, named *flavours*, and are split into three generations. The first generation consists in the *up* and the *down* quark, the former with $Q = +2/3$ and $T_3 = +1/2$, while the latter $Q = -1/3$, $T_3 = -1/2$ and a slightly lower mass. The next two generations are copies of the first one with increasing mass, with a pair of a *up*-type quark and a *down*-type quark. The second family consists in *charm* and *strange* quarks, and the third of *top* and *bottom* quarks. In addition, all of the six quark flavours have antimatter states with the same mass, but opposite quantum numbers, as an example, an anti-*up*-type quark has $Q = -2/3$, $T_3 = -1/2$ and can carry anti-*red* colour.

Leptons are also similarly divided in six different types and in three separate generations named *electron* (e), *muon* (μ) and *tau* (τ), also with increasing mass.

Each generation contains a lepton with $Q = -1$ and $T_3 = +1/2$ named after its generation, and an associated electrically neutral lepton with $T_3 = -1/2$ named neutrino (ν). The neutrino is assumed to be massless in the formulation of the SM, however the phenomena of neutrino oscillations is experimental proof of them actually having very small, but non-zero, mass values. This apparent failure of the theory is discussed in Section 1.2.4. As before, the associated antimatter states have the same mass but opposite quantum numbers.

All the stable SM matter in the universe is constituted by the massive particles of the first generations of quarks and leptons, as the heavier versions eventually decay to lighter ones through their disclosed interactions. While it is possible to observe free leptons, quarks exist only in bound states, or hadrons, like the neutron or the proton. This is a feature of the strong interaction under the name of confinement, discussed in Section 1.1.3. Only colour-less bounded states are observable then, and can be built from three quarks with overall half-spin, named baryons, or by two quarks with integer spin, named mesons.

In the context of particle physics, the formulation of the classical Lagrangian, $\mathcal{L}$, is used to describe physics systems. A generic free fermion field ψ with mass m, can be described by the Dirac Lagrangian,

$$\mathcal{L} = \bar{\psi}(i\gamma^{\mu}\partial_{\mu} - m)\psi, \tag{1.2}$$

where γ^{μ} are Dirac matrices and ∂_{μ} is the four-momentum derivative.

Bosons

Particles with integer spin are referred to as bosons. The bosonic sector with spin-1 gauge fields are force carriers that naturally follow from imposing the requirement of local gauge invariance on Equation 1.2 under symmetry groups, in this case Equation 1.1. In Section 1.1.2 the nature and origin of the gauge bosons will be detailed. Table 1.2 presents a summary of the bosons of the SM.

Table 1.2: Table of the different bosons of the SM with their mass and electric charge according to the Particle Data Group [16]. The Higgs boson has spin 0 and does not mediate an interaction, while the rest have spin 1 and mediate an interaction.

Name	Mass [GeV]	Charge	Interaction
Photon (γ)	0	0	Electromagnetic
Z	91.1876 ± 0.0021 GeV	0	Weak
$W^{\pm}$	80.377 ± 0.012 GeV	±1	
Gluon (g)	0	0	Strong
Higgs	125.25 ± 0.17 GeV	0	-

In summary, the photon (γ) is the carrier of the electromagnetic force, being a massless and electrically neutral particle. The weak force carriers are the W^+, W^- and Z bosons, all massive with the Z boson being electrically neutral and the $W^{\pm}$

with either $Q = \pm 1$. Gluons (g) are the strong force carriers which are massless and with no electric charge. Instead, there are eight different gluons representing each possible colour exchange.

The SM also includes a neutral spin-0 particle, or *scalar*, the Higgs boson. The Higgs field is responsible for all SM particles acquiring mass through the Higgs mechanism, as described in Section 1.1.5. The kinematics of a generic scalar ϕ with mass m, is described by the Klein-Gordon Lagrangian,

$$\mathcal{L} = \frac{1}{2}\partial^{\mu}\phi\partial_{\mu}\phi - m^2\phi^2 \tag{1.3}$$

Charged scalars can be described instead through a complex field and the expression of the Lagrangian is slightly modified,

$$\mathcal{L} = \partial^{\mu}\phi\partial_{\mu}\phi^{*} - m^2\phi\phi^{*} \tag{1.4}$$

Vector fields A^{μ}, which represent spin-1 bosons, are described by the Proca Lagrangian,

$$\mathcal{L} = -\frac{1}{4}F^{\mu\nu}F_{\mu\nu} + \frac{1}{2}m^2A^{\mu}A_{\mu} \tag{1.5}$$

with $F^{\mu\nu} = \partial^{\mu}A_{\nu} - \partial^{\nu}A_{\mu}$ the field strength tensor. In the case of massless particles, the previous expression with $m = 0$ is known as the Maxwell Lagrangian.

1.1.2 Interactions of the Standard Model

The Lagrangian of the SM is defined to be locally invariant to the Equation 1.1 symmetry group, condition that generates and defines the interactions of the corresponding particles as representations of the symmetry transformations. For a generic Lagrangian, the physical system can have symmetries, so its Lagrangian is invariant under different kind of transformations. These transformations can be time-space independent, called global transformations, or dependent, called gauge or local transformations. Any invariant transformation of a Lagrangian describes a physical system which conserves a physical quantity, as described by the Noether theorem [17]. Then, the interactions are introduced in the Lagrangian as additional terms by promoting an already existing global symmetry, ϕ, of the Lagrangian to a local gauge symmetry, $\phi(x)$. The physical motivation behind introducing gauge symmetries is to be able to describe vector bosons in QFT. The procedure expands the theory with additional fields that mediate the resulting interactions, which properties depend on the characteristics of the symmetry group.

An example of the process is shown in the following, to afterwards derive the SM interactions of the strong and electroweak sectors.

Gauging a symmetry to interaction

A general global transformation θ which acts on the field ψ is described as,

$$\psi \longrightarrow e^{ig\theta^a T^a}\psi \tag{1.6}$$

with g the coupling constant and T^a the generators of the Lie group associated to the transformation (like $SU(n)$ or $U(n)$), with a ranging from 1 to $n^2 - 1$, for the corresponding number of the Lie algebra, $n > 1$. The generators can be characterised by their commutation relation,

$$[T^a, T^b] = if^{abc}T^c \tag{1.7}$$

where f^{abc} are the structure constants of the group. Following Noether's theorem, there are as many conserved quantities as generators of the Lagrangian's symmetries. As an example, it is straightforward to see that a Lagrangian like Equation 1.2 is invariant to a $U(1)$ transformation where θ is just a constant and hence, a constant phase change. One can obtain the current, j^μ, that is conserved, $\partial_\mu j^\mu = 0$,

$$j^\mu = \bar{\psi}\gamma^\mu\psi \tag{1.8}$$

and the conserved charge,

$$Q = \int \mathrm{d}^3x j^0 = \int \mathrm{d}^3x \psi^\dagger\psi \tag{1.9}$$

With some algebra and introducing solutions in momentum space, ψ can be interpreted as annihilating a fermion and creating an anti-fermion ($\psi^\dagger$ the other way around) in the Fock space and then, this product becomes the difference of the number of fermion and anti-fermion leading to the conservation of the fermion number.

Promoting the global symmetry to a local symmetry is done by introducing locality in the θ transformation, $\theta \longrightarrow \theta(x)$, which introduces new $\partial_\mu\theta$ terms in the Lagrangian. A way to counter the new terms and, hence, keep the Lagrangian invariant, is to introduce gauge vector fields A^a_μ, following Yang-Mills theory [18]. In the most generalised approach, there have to be as many A^a_μ as generators of the symmetry, that transform as,

$$A^a_\mu \longrightarrow A^a_\mu + \partial_\mu\theta^a + gf^{abc}A^b_\mu\theta^c \tag{1.10}$$

Note that the last term proportional to the structure constant is relating the gauge field to the conserved symmetry charge. The next step is to replace the standard derivative in the Lagrangian by the covariant derivative,

$$D_\mu \equiv \partial_\mu - igT^a A^a_\mu \tag{1.11}$$

The final ingredient is to complete the Lagrangian with the the kinematic Lagrangian for the massless vector fields, the Maxwell Lagrangian from Equation 1.5 with a slightly different field strength tensor,

$$F^a_{\mu\nu} = \partial_\mu A^a_\nu - \partial_\nu A^a_\mu + g f^{abc} A^b_\mu A^c_\nu \tag{1.12}$$

The last term is present only for non-abelian symmetry groups, since it is proportional to the structure constants, and has huge consequences in the resulting interactions as discussed in the next Section. Another remark is that the gauge fields have to be massless, as a mass term proportional to $A^c_\mu A^{\mu c}$ is not gauge invariant.

As an example, the promotion of the global $U(1)$ symmetry seen in Equation 1.2 results in the upgraded Lagrangian,

$$\begin{aligned} \mathcal{L} &= \bar{\psi}(i\gamma^\mu D_\mu - m)\psi - \frac{1}{4}F_{\mu\nu}F^{\mu\nu} \\ D_\mu &\equiv \partial_\mu - igA_\mu \\ F_{\mu\nu} &\equiv \partial_\mu A_\nu - \partial_\nu A_\mu \end{aligned} \tag{1.13}$$

introducing just one massless gauge field that interacts with the field ψ. The interaction term between the two fields is $g\bar{\psi}\gamma^\mu A_\mu \psi$, hidden in the covariant derivative definition and proportional to the coupling constant g.

The Lagrangian of the SM is built from imposing local invariance under $SU(3)_C$ transformations, which leads to strong interactions; and $SU(2)_L \times U(1)_Y$ transformations, which brings EW interactions,

$$\mathcal{L}_{SM} = \mathcal{L}_{QCD} + \mathcal{L}_{EW} \tag{1.14}$$

After this introduction on field theory, the theories of the two orthogonal sectors can now be described and then, the mechanism to introduce mass terms in the Lagrangian, the spontaneous symmetry breaking.

1.1.3 Quantum Chromodynamics

The quantum field theory that describes quarks, gluons and their interactions is named *quantum chronodynamics*. Each quark has an internal degree of freedom, the colour charge, and it is defined by a triplet of fields,

$$q = \begin{pmatrix} q_{\text{red}} \\ q_{\text{blue}} \\ q_{\text{green}} \end{pmatrix} \tag{1.15}$$

where each of the components is a Dirac spinor associated to the corresponding colour state (red, blue and green). In addition, there are a total of six quarks, so the fields are labelled as $q_{f\alpha}$ with f indicating the quark flavour ($f = u, d, c, s, t, b$) and α the colour. Note that there is an anti-quark of each flavour carrying an anti-colour charge.

The theory is based on the $SU(3)$ symmetry group, whcih algebra is characterised by the non-abelian commutation relation from Equation 1.7 with a total of eight generators, T^a. The generators can be written as $T^a = \lambda^a/2$ where λ^a denote the Gell-Mann matrices [19]. Because of the eight generators, the interaction is mediated by a total of eight gauge bosons, called gluons G^a_μ. There are different matrix representation for the colour states of the gluons, following with the Gell-Mann matrices, taking,

$$\lambda^1 = \begin{pmatrix} 0 & 1 & 0 \\ 1 & 0 & 0 \\ 0 & 0 & 0 \end{pmatrix} \tag{1.16}$$

and applying it to a general quark triplet like Equation 1.15, it can be seen that the transformation switches the red and blue charges. To do so, the gluon has to carry a colour/anti-colour pair, to be able to "remove" the red charge (r) and "add" the blue charge (b), and the other way around. There are nine possible combinations of colour/anti-colour pairs, which can be used to re-write the λ^1 transformation as,

$$\frac{r\bar{b} + b\bar{r}}{\sqrt{2}} \tag{1.17}$$

known as the first state of the gluon colour octet. The rest of the states are equivalent to the other Gell-Mann matrices and all conserve the three different colour flows.

The QCD Lagrangian can be obtained from modifying the the Dirac Lagrangian (Equation 1.2) to achieve gauge invariance under $SU(3)_C$ transformations, following the definitions from Section 1.1.2. The resulting Lagrangian is,

$$\begin{aligned} \mathcal{L}_{QCD} &= i \sum_f \bar{q}_f \gamma^\mu D_\mu q_f - \frac{1}{4} G^a_{\mu\nu} G^{a\ \mu\nu} \\ D_\mu &\equiv \partial_\mu - i g_s T^a G^a_\mu \\ G^a_{\mu\nu} &\equiv \partial_\mu G^a_\nu - \partial_\nu G^a_\mu + g_s f^{abc} G^b_\mu G^c_\nu \end{aligned} \tag{1.18}$$

with g_s being the strong force coupling constant and where the covariant derivative has been introduced with the G^a_μ gluons fields, together with the kinematic term for the gluons, with the gluon tensor $G^a_{\mu\nu}$. As described in Section 1.1.2, gluons are massless because the term in the Lagrangian is not gauge invariant. Notice that the masses of the quarks are also not present, not because it would break the symmetry, but for convention. The masses in the SM come from the electro-weak sector. Another remark is that the addition of a charge conjugation and parity symmetry

(CP) violating interaction term is allowed under local gauge invariance, but such an interaction has been experimentally observed to be effectively zero [20].

The possible interactions in the Lagrangian are shown in Figure 1.1, consisting of couplings between quarks and gluons[1], and three- and four-point gluon self-interactions. As foreshadowed in Section 1.1.2, for non-abelian groups the gauge bosons have the self-interacting terms in the tensor.

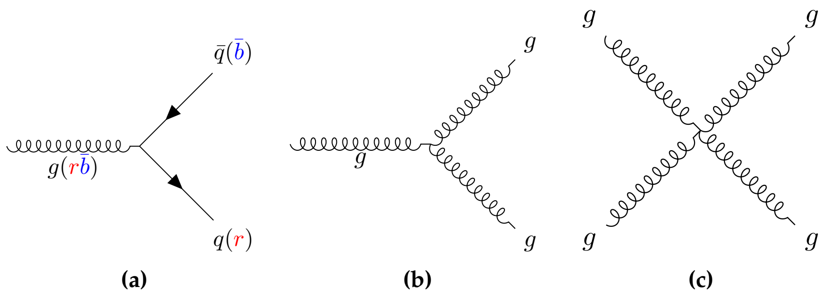

Figure 1.1: Vertices allowed in QCD: (a) quark-gluon coupling, (b) three-point gluon self-coupling, and (c) four-point gluon self-coupling. The color charge is depicted in the the quark-gluon vertex to depict an example of the interaction.

There are two more important characteristics of this theory: asymptotic freedom and confinement [21, 22]. Asymptotic freedom refers to the fact that at very high energies (in momentum transfer), or short distances, quarks and gluons interact weakly with each other allowing predictions to be obtained using perturbation theory. Confinement is the name given to the impossibility of directly observing quarks, only confined in hadrons, which are colorless composite states[2]. The idea is that for high distances, the strong coupling becomes larger, so when the distance between two quarks is increased, the energy of the gluon field is larger, up to the point to create from the vacuum a quark/anti-quark pair and thus forming a new hadron. These characteristics arise from the non-abelian nature of the symmetry, which prompt the coupling to decrease with the energy of the interaction.

Running coupling

To understand the fact that the couplings can vary with the energy, the QFT renormalisation and regularisation procedures have to be introduced. The quantity known as the matrix amplitude has to be computed for the prediction of physical quantities of a given process. Observables are actually proportional to the square sum of the amplitude of every possible Feynman diagram that yields the same initial and final particles of the process to be predicted. However, the computation in diagrams with loops spawns the integration for all possible four-momentum of the virtual particles involved, which are divergent. Nevertheless, these divergencies can be isolated with regularisation techniques, which renders them finite by introducing

[1] Equivalent to the interaction obtained from the gauge $U(1)$ symmetry.
[2] Color singlets are quantum states that are invariant under all eight generators of $SU(3)$, and therefore carry vanishing values of all colour conserved charges.

a parameter Λ such that only for a given value of the parameter the divergence is recovered. This allows the computation of any quantity in terms of the *bare* quantities appearing in the Lagrangian, such as masses and couplings, along the regularisation parameter. The other key point is renormalisation, from the idea that the physical quantities measured in experiments (masses and couplings), are different from the bare quantities (masses and couplings that appear in the lagrangian). Therefore, one has the freedom to apply renormalisation conditions which cause the expressions to depend only on the physical quantities if the theory is renormalisable, removing the divergent sources.

As an example, to compute the gluon two-point function, an infinite sum of loop contributions is needed,

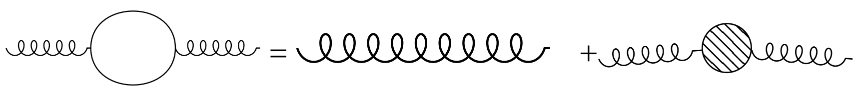

(1.19)

Focusing on the one loop contribution, the result is obtained at first order from three different diagrams,

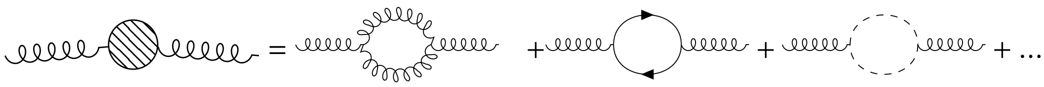

(1.20)

which includes the loop involving gluons, quarks and a third one with a new propagator, the ghost. This propagator is a regularisation artifact to compensate unphysical degrees of freedom[3]. Focusing on the gluon loop contribution,

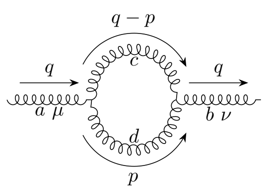

(1.21)

prompts in its computation with Feynman rules a badly divergent integral,

$$\frac{1}{2}g_s^2 f^{acd} f^{bcd} \int \frac{d^4p}{(2\pi)^4} \frac{1}{(q-p)^2+i\epsilon} \frac{1}{p^2+i\epsilon} \left[g^{\mu\alpha}(p-2q)^{\beta} + g^{\alpha\beta}(q-2p)^{\mu} + g^{\beta\mu}(p+q)^{\alpha}\right] \left[\delta^{\nu}_{\alpha}(p-2q)_{\beta} + g_{\alpha\beta}(q-2p)^{\nu} + \delta^{\nu}_{\beta}(p+q)_{\alpha}\right] \tag{1.22}$$

which can be worked around with a regularisation constant μ,

[3] There are other methods to avoid the unphysical degrees of freedom, as choosing a physical gauge in the axial direction.

$$\int \frac{d^4p}{(2\pi)^4} \to \int \frac{d^Dp}{(2\pi)^D}\mu^{2\varepsilon}.$$

and $D = 4 - 2\varepsilon$ with later $\varepsilon \longrightarrow 0$. After the computation of all main contributions, the divergent term can be summarised as,

$$\frac{g_s^2}{24\pi}\left[11n_c - 2n_f\right]\frac{1}{\epsilon} + \mathcal{O}(g_s^4) \tag{1.23}$$

with n_c the number of colours, n_f the number of quark flavours and $\varepsilon \longrightarrow 0$ the condition to recover the original divergence. Hence the bare coupling constant can be rewritten to account for this divergence, completing the regularisation process for the gluon self-energy.

The final strong coupling constant is commonly given by,

$$\alpha_s(Q^2) = \frac{12\pi}{(11n_c - 2n_f)\log\frac{Q^2}{\Lambda^2_{\mathrm{QCD}}}} \tag{1.24}$$

which depends on the energy scale Q at which is evaluated and Λ_{QCD} the infrared cutoff scale which sets the validity of the perturbative regime of QCD. As $n_c = 3$, for n_f<16 the coupling constant decreases with the energy scale, the very feature of QCD that causes asymptotic freedom and confinement.

1.1.4 Electroweak theory

The quantum field theory that describes both the electromagnetic and weak interactions is named *electroweak* theory. The theory is based on the $SU(2)_L \otimes U(1)_Y$ symmetry group[4], which is a product that yields a non-abelian group, like $SU(3)_C$, and chiral. It will spawn four mediators, as the number of generators. The symmetry spontaneously breaks down through *symmetry breaking*, giving rise to the electromagnetic interaction, mediated by the photon, and to the weak interaction, mediated by the Z and $W^\pm$ bosons. This process is described by the *EW symmetry breaking* (EWSB), which occurs at ~100 GeV, defined as the EW scale, and after which only the $U(1)_Q$ symmetry is unbroken, . The process of the EWSB, and the resulting effects are described in more detail in Section 1.1.5.

The interactions for the EW sector can be obtained following the procedure described in general in Section 1.1.2, already used in Section 1.1.3 for QCD. First, only left-handed fermion fields interact via the weak interaction[5], transforming as doublets under $SU(2)_L$, whereas right-handed fermion fields do not interact weakly and thus transform as singlets,

[4] L refers to the left-handed chirality and Y to the weak hypercharge
[5] As a consequence, parity can be violated in weak interactions [23, 24].

$$\begin{aligned}\psi_L^i &= \begin{pmatrix} \ell_L^i \\ \nu_L^i \end{pmatrix}, \begin{pmatrix} u_L^i \\ d_L^i \end{pmatrix} \\ \psi_R^i &= \ell_R^i, u_R^i, d_R^i\end{aligned} \tag{1.25}$$

with i corresponding to the number of the generation. Fields with subscripts L/R are left- and right-handed fields that can be defined through the chirality operators P_L and P_R, projecting a generic field into only its left- and right-handed components, respectively,

$$\begin{aligned}\psi_L &= P_L\psi = \frac{1}{2}(1-\gamma_5)\psi \\ \psi_R &= P_R\psi = \frac{1}{2}(1+\gamma_5)\psi\end{aligned} \tag{1.26}$$

with γ_5 defined from the Dirac matrices $\gamma_5 \equiv i\gamma^0\gamma^1\gamma^2\gamma^3$. Notice that there are no right-handed fields associated to the neutrinos. This convention exists to avoid the prediction of right-handed neutrinos, which would not interact with any of the forces described in the SM.

The $SU(2)_L$ group consists of three generators $\hat{T}_i$, which can be written as $\hat{T}_i = \sigma_i/2$ where σ_i denotes the Pauli matrices. Also, the quantum number associated is the weak isospin, T. On the other side, the $U(1)_Y$ group introduces the weak hypercharge quantum number, Y. After EWSB, the Gell-Mann-Nishijima equation relates Y to the third component of the weak isospin operator, T_3 and the electric charge Q,

$$Q = Y + T_3 \tag{1.27}$$

Regarding the EW Lagrangian, four gauge fields need to be introduced to achieve invariance under the $SU(2)_L \otimes U(1)_Y$: $W^i_{\mu\nu}$ (i=1,2,3) from $SU(2)_L$, and B_μ from $U(1)_Y$. The resulting Lagrangian is,

$$\begin{aligned}\mathcal{L}_{EW} &= i\sum_{f=l,q}\bar{f}(\gamma^\mu D_\mu)f - \frac{1}{4}W^i_{\mu\nu}W^{i\ \mu\nu} - \frac{1}{4}B_{\mu\nu}B^{\mu\nu} \\ D_\mu &\equiv \partial_\mu - ig\frac{\sigma}{2}W^i_\mu - ig'YB_\mu \\ W^i_{\mu\nu} &\equiv \partial_\mu W^i_\nu - \partial_\nu W^i_\mu + g\epsilon^{ijk}W^j_\mu W^k_\nu \\ B_{\mu\nu} &\equiv \partial_\mu B_\nu - \partial_\nu B_\mu\end{aligned} \tag{1.28}$$

with ϵ^{ijk} the Levi-Civita symbol, an antisymmetric tensor defined as $\epsilon^{ijk}\epsilon_{imn} = \delta^j_m\delta^k_n - \delta^j_n\delta^m_k$ with $i,j,k,l,m,n \in [1,2,3]$. Also, the $W^i_{\mu\nu}$ and $B_{\mu\nu}$ field tensors are defined to introduce the additional kinetic terms to the Lagrangian. The former contains a quadratic piece, due to the non-abelian nature of $SU(2)_L$, hence the full

Lagrangian contains cubic and quartic self-interactions, as seen for the gluons in QCD. In contrast, the coupling constant g increases rapidly with the energy scale. As encountered before, mass terms for the gauge boson would break the gauge invariance. In this case, terms for the fermion masses would also break the symmetry as they would mix left- and right-handed fields, which transforms distinctively under $SU(2)_L$.

Summing all the interactions described, the SM Lagrangian for all the fermions before EWSB becomes,

$$\begin{aligned}\mathcal{L}_{SM} &= \sum_{f} \sum_{\psi=L,e_R,Q_L,u_R,d_R} i\bar{\psi}^f \gamma^\mu D_\mu \psi^f \\ &- \frac{1}{4}G^a_{\mu\nu}G^{a\_\mu\nu} - \frac{1}{4}W^i_{\mu\nu}W^{i\_\mu\nu} - \frac{1}{4}B_{\mu\nu}B^{\mu\nu} \\ D_\mu &= \partial_\mu - ig_s T^a G^a_\mu - ig\frac{\sigma^i}{2}W^i_\mu - ig'YB_\mu\end{aligned} \tag{1.29}$$

1.1.5 Spontaneous symmetry breaking and the Higgs mechanism

The model described so far cannot reproduce measured results, first of all the different fermions and the weak force mediators have mass and second, the $SU(2)_L \times U(1)_Y$ symmetry is not preserved in nature. Even if somehow the EW gauge bosons are allowed to have mass, it leads to the lack of renormalisability and the violation of unitarity. Renormalisation is a collection of techniques that allows the computation of measurable observables in QFT, managing the different sources of infinities within the theory like those from self-interactions. Unitarity is needed more in general in quantum mechanics, to ensure proper time-evolution predictions of a quantum state. The longitudinal component of the massive boson is the cause of the problem, as in a boosted frame in which $p^\mu = (p^0, 0, 0, |\mathbf{p}|)$, the parallel polarisation component of a massive boson is $\epsilon_\mu = (|\mathbf{p}|/m, 0, 0, p^0)$, growing indefinitely with the energy of the system. When computing the cross-section of the corresponding boson scattering, the value will indefinitely grow breaking the mentioned unitarity. If computed explicitly for the $W^\pm$ bosons, the energy scale where this happens is around the TeV scale, pointing to a fundamental problem in the theory to describe that scale.

The solution is provided by the EWSB and the Higgs-Englert-Brout mechanism, discussed next, after showing the spontaneous symmetry breaking process for a simple gauge theory.

How to break a symmetry

Spontaneous symmetry breaking is a phenomenon where a symmetry of the theory is unstable and the vacuum, or fundamental state, is degenerate. In the process, new interactions appear and a field obtains a non-zero vacuum expectation value.

The topic is broad as there are many symmetries and representations to potentially break, to illustrate the mechanism for the SM, lets consider a system with a scalar field ϕ, a gauge field A_μ, and the following Lagrangian with a gauge symmetry,

$$\begin{aligned} \mathcal{L} &= (D^\mu\phi)^\dagger D_\mu\phi - V(\phi) - \frac{1}{4}F_{\mu\nu}F^{\mu\nu} \\ D_\mu &\equiv \partial_\mu - igA_\mu \\ F_{\mu\nu} &\equiv \partial_\mu A_\nu - \partial_\nu A_\mu \end{aligned} \tag{1.30}$$

with a general potential $V(\phi)$ given by,

$$V(\phi) = \frac{1}{2}\mu^2\phi^\dagger\phi + \frac{1}{4}\lambda(\phi^\dagger\phi)^2 \tag{1.31}$$

with the real parameters μ^2 and λ relating respectively to the mass term and the strength of the self-interaction. There are two sensible ranges for these parameters, depicted in Figure 1.2, the first one is the case $\lambda, \mu^2 > 0$, similar to the previous theories and only one solution in the minimisation. The second one is for $\lambda > 0$ and $\mu^2 < 0$, where the $\mu^2\phi^\dagger\phi$ term cannot be understood as a mass term and the solution $\phi = 0$ is a local maximum, physically unstable. The minimum of the potential is degenerate and identified by the complex plane circle, $\phi^\dagger\phi = v^2/2$ with $v^2 \equiv -\mu^2/\lambda$ and

$$\phi = ve^{-i\theta} \tag{1.32}$$

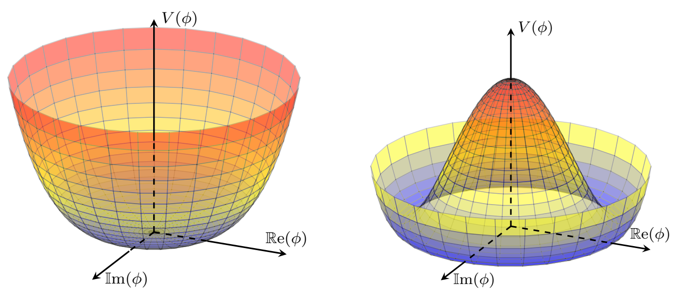

Figure 1.2: Shape of the potential $V(\phi)$ for $\lambda > 0$ and (a) $\mu^2 > 0$ or (b) $\mu^2 < 0$.

The symmetry is broken spontaneously when the system choses the fundamental state. Suppose $\phi = 0$, then the *Vacuum Expectation Value* (VEV) of ϕ is set to,

$$\langle 0|\phi|0\rangle = \frac{v}{\sqrt{2}} \tag{1.33}$$

Next, lets suppose the following change of variables to center the new fundamental state,

$$\phi(x) = \left(\frac{v + \eta(x)}{\sqrt{2}}\right) e^{i\zeta(x)/v} \tag{1.34}$$

the Lagrangian can be expressed as,

$$\begin{aligned} \mathcal{L} &= \frac{1}{2}(\partial_\mu \eta)^2 + \frac{1}{2}(\partial_\mu \zeta)^2 - \frac{1}{4}F_{\mu\nu}F^{\mu\nu} \\ &+ \mu^2\eta^2 + \frac{1}{2}g^2v^2 A_\mu A^\mu - gvA\mu\partial^\mu\zeta + \text{ interactions} \end{aligned} \tag{1.35}$$

which now contains the η and ζ fields, additional to the gauge A_μ. Also, square terms appear for η and A_μ, which can be identified as mass terms, $\frac{m_\eta}{2}\eta^2$ and $\frac{m_A}{2}A_\mu A^\mu$, resulting in $m_\eta = \sqrt{-2\mu^2}$ and $m_A = gv$. $\zeta(x)$ is massless and a particular resulting type of field named *Goldstone boson*, which the *Goldstone theorem* predicts. The theorem states that a massless boson appears for every symmetry that the VEV spontaneously breaks. In this abelian case, the VEV is not invariant under the $U(1)$ transformation. $\zeta(x)$ does not appear explicitly in the potential, therefore can take any value without affecting the energy of the system, which is not very physical. In addition, it appears in an estrange mixing term with A_μ, $-gvA_\mu\partial^\mu\zeta$. A way to remove this annoyance is to choose the gauge,

$$\begin{aligned} \phi &\rightarrow \phi' = e^{-i\zeta/v}\phi \\ A_\mu &\rightarrow A'_\mu = A_\mu - \frac{1}{gv}\partial_\mu\zeta \end{aligned} \tag{1.36}$$

together with the previous change of variable for ϕ. Essentially the gauge freedom of the Lagrangian is being used to remove ζ, which becomes the longitudinal component of the transformed gauge boson A_μ. The gauge chosen is the so-called *unitary gauge*, which makes the physical content of the Lagrangian explicit[6].

In summary, this process of acquiring mass by means of absorbing a Goldstone boson is known as the *Higgs mechanism*.

The Higgs-Englert-Brout Mechanism in the Electroweak Sector

The Higgs-Englert-Brout mechanism [25–27] solved the contradictions found between massive particles and the requirement of gauge invariance. The mechanism is based in a spontaneous symmetry breaking of the $SU(2)_L \otimes U(1)_Y$ to $U(1)_{EM}$, giving mass to the different particles involved in the EW interactions except the photon. A similar procedure can be applied to the EW Lagrangian derived in Equation 1.29, first introducing an isospin doublet (Y=+1/2) of complex scalar fields Φ, the Higgs field,

[6] As a parallel, the ghost gluons in the context of regularisation also remove the problematic unphysical degrees of freedom.

$$\Phi \equiv \begin{pmatrix} \phi^+ \\ \phi^0 \end{pmatrix} = \frac{1}{\sqrt{2}} \begin{pmatrix} \phi_1 + i\phi_2 \\ \phi_3 + i\phi_4 \end{pmatrix} \tag{1.37}$$

where ϕ^+ corresponds to an electrically charged field (T_3=+1/2) and ϕ^0 to a neutral one (T_3=-1/2). This field transforms under $SU(2)_L$ and its Lagrangian, the Higgs Lagrangian,

$$\mathcal{L}_\Phi = (D_\mu \Phi)^\dagger (D^\mu \Phi) - V(\Phi) \tag{1.38}$$

with the same covariant derivative as in Equation 1.29 and the Higgs potential given by,

$$V(\Phi) = \mu^2 \Phi^\dagger \Phi + \lambda (\Phi^\dagger \Phi)^2 \tag{1.39}$$

which shape depends on the parameters μ^2 and λ. As seen before, choosing the case where $\lambda > 0$ and $\mu^2 < 0$, the potential at $\Phi = 0$ is unstable and a continuous collection of possible minimum values appear, defined by the circle,

$$\Phi^\dagger \Phi = \frac{1}{2} \frac{-\mu^2}{\lambda} \equiv \frac{1}{2} v^2 \tag{1.40}$$

Following, the spontaneous symmetry breaking with the choice of the new vacuum state,

$$\langle 0|\Phi|0\rangle = \frac{1}{\sqrt{2}} \begin{pmatrix} 0 \\ v \end{pmatrix} \tag{1.41}$$

This vacuum is not invariant to any of the $SU(2)_L$ and the $U(1)$ transformations, however, the $Q = T_3 + Y$ transformation is not affected,

$$Q \langle 0|\Phi|0\rangle = \frac{1}{2\sqrt{2}} \sigma_3 \begin{pmatrix} 0 \\ v \end{pmatrix} + \frac{1}{2\sqrt{2}} Y \begin{pmatrix} 0 \\ v \end{pmatrix} = \frac{1}{2\sqrt{2}} \left[\begin{pmatrix} 0 \\ -v \end{pmatrix} + \begin{pmatrix} 0 \\ v \end{pmatrix} \right] = \begin{pmatrix} 0 \\ 0 \end{pmatrix} \tag{1.42}$$

The field is rewritten in the unitary gauge, which automatically removes the extra nonphysical Goldstone bosons,

$$\Phi(x) = \frac{1}{\sqrt{2}} \begin{pmatrix} 0 \\ v + H(x) \end{pmatrix} \tag{1.43}$$

where $H(x)$ is centered around the vacuum state. With this change the Higgs potential becomes,

$$V(\Phi) = \frac{1}{4} \lambda v^2 H^2 + \frac{1}{4} \lambda v H^3 + \frac{1}{16} \lambda H^4 \tag{1.44}$$

spawning the Higgs boson mass $m_H^2 = \lambda v^2/2 = -\mu^2/2$, in the quadratic H term. The cubic and quartic terms constitute the three- and four-point Higgs boson self-interactions.

The EWSB generates new interactions and mass terms for the different particles involved in the EW interactions. Gluons are not affected as the scalar field is a doublet and does not transform under $SU(3)$. The effects on the boson and fermion sectors of the SM are discussed in the following, individually.

Boson sector

The gauge boson masses spawn from the covariant derivative, $(D_\mu\Phi)^\dagger(D^\mu\Phi)$, which includes the gauge fields. Expanding,

$$\mathcal{L}_{mass} = \frac{v^2}{8} V_\mu \begin{pmatrix} \begin{matrix} g^2 & 0 \\ 0 & g^2 \end{matrix} & 0_{2\times2} \\ 0_{2\times2} & \begin{matrix} g^2 & -gg' \\ -gg' & g'^2 \end{matrix} \end{pmatrix} V^\mu \tag{1.45}$$

with $V_\mu = \begin{pmatrix} W_\mu^1 & W_\mu^2 & W_\mu^3 & B_\mu \end{pmatrix}$. Diagonalising the matrix, the next eigenvectors are found,

$$\begin{aligned} A_\mu &\equiv \sin\theta_W W_\mu^3 + \cos\theta_W B_\mu \\ Z_\mu &\equiv \cos\theta_W W_\mu^3 - \sin\theta_W B_\mu \end{aligned} \tag{1.46}$$

where the Weinberg angle, or weak mixing angle, is defined by $\tan\theta_W \equiv g'/g$. The corresponding eigenvalues, the square masses, for the A_μ and Z_μ fields are zero and $v^2(g^2+g'^2)/8$. On the other side, W_μ^1 and W_μ^2 are well defined mass states but not charge states. This is due T_1 and T_2 being not diagonal, connecting the different states of T_3 (hence of Q). The operator $T_\pm = T_1 \mp iT_2$ can be defined, which increases or decreases one unit of T_3 (hence of Q). In addition, the fields can be redefined,

$$W_\mu^\pm = \frac{1}{\sqrt{2}}(W_\mu^1 \mp iW_\mu^2) \tag{1.47}$$

In summary the Lagrangian in Equation 1.45 can now be written as

$$\mathcal{L}_{mass} = \frac{g^2v^2}{4} W_\mu^+ W^{-\mu} - \frac{v^2}{8}(g^2+g'^2) Z_\mu Z^\mu \tag{1.48}$$

where the mass terms of the different bosons can be identified,

$$\begin{aligned} m_A &= 0 \\ m_Z &= \frac{v}{2}\sqrt{g^2 + g'^2} \\ m_W &= \frac{vg}{2} = m_Z \cos\theta_W \end{aligned} \tag{1.49}$$

Note that the remaining symmetry after breaking $SU(2)_L \otimes U(1)_L$ is $U(1)_{EM}$. The associated A_μ field is massless, the photon, which is a combination of the W^3_μ and B_μ fields. The associated quantum number, the electric charge, has been defined previously in the chapter, $Q = T_3 - Y$.

Regarding interactions, the covariant derivative can be expressed in terms of the new bosons,

$$\partial_\mu - igW^3_\mu = \partial_\mu - ig\sin\theta_W A_\mu - ig\cos\theta_W Z_\mu \tag{1.50}$$

where the electromagnetic coupling constant e can be defined as $e = g\sin\theta_W$. In addition, the field tensors can be rewritten as,

$$\begin{aligned} W^3_{\mu\nu} &= \partial_\mu W^3_\nu - \partial_\nu W^3_\mu - ig(W^+_\mu W^-_\nu - W^+_\nu W^-_\mu) \\ &= \sin\theta_W F_{\mu\nu} + \cos\theta_W Z_{\mu\nu} - ig(W^+_\mu W^-_\nu - W^+_\nu W^-_\mu) \\ B_{\mu\nu} &= \cos\theta_W F_{\mu\nu} - \sin\theta_W Z_{\mu\nu} \end{aligned} \tag{1.51}$$

where the field strength tensors for the photons and the Z boson, $F_{\mu\nu}$ and $Z_{\mu\nu}$ are defined.

Fermion sector

The procedure required to acquire the fermion masses is more complicated than for the gauge bosons. Instead of just expanding the kinematic term with the new Higgs field, Yukawa [28] interactions that couple left- and right-handed fermions with the Higgs need to be introduced.

As seen in this chapter, only $q^i_{\alpha L}$ and l^i_L fields are $SU(2)_L$ doublets,

$$q^i_{\alpha L} = \begin{pmatrix} u^i_{\alpha L} \\ d^i_{\alpha L} \end{pmatrix},\ l^i_L = \begin{pmatrix} \nu^i_L \\ \ell^i_L \end{pmatrix} \tag{1.52}$$

where the i refers to the generation and α to the colour. It has been already pointed out that is not possible to construct a well defined $mf^\dagger f$ term that transforms under the SM group, necessary for gauge invariance.

The solution is provided by introducing Yukawa interactions between the fermion fields and the Higgs field Φ, also a doublet under $SU(2)$,

$$\mathcal{L}_{Yukawa} = -y^{ab}\bar{q}^{a}_{\alpha\ L}\Phi d^{b}_{\alpha\ R} - y'^{ab}\bar{q}^{a}_{\alpha\ L}\tilde{\Phi} u^{b}_{\alpha\ R} - y''^{ab}\bar{l}^{a}_{L}\Phi \ell^{b}_{R} + \text{ h.c} \tag{1.53}$$

where y, y′ and y″ are the Yukawa matrices, 3×3 matrices with one dimension for each generation. Also, $\tilde{\Phi} \equiv i\sigma_2\Phi^*$. Note that there is no second term for the leptons, as the SM does not contemplate the right handed neutrino, ν_R. Also, this Lagrangian breaks explicitly the chiral symmetry but yields a singlet representation, safe for gauge invariance. Next, writing the field Φ in terms of the unitary gauge as in the EWSB, $\phi^0(x) = v + H(x)$,

$$\begin{aligned}
\mathcal{L}_{Yukawa} &= -\frac{1}{\sqrt{2}}(v+H)y^{ab}\bar{q}^{a}_{\alpha\ L}d^{b}_{\alpha\ R} - \frac{1}{\sqrt{2}}(v+H)y'^{ab}\bar{q}^{a}_{\alpha\ L}u^{b}_{\alpha\ R} \\
&- \frac{1}{\sqrt{2}}(v+H)y''^{ab}\bar{l}^{a}_{L}\ell^{b}_{R} + \text{ h.c} \\
&= -\frac{1}{\sqrt{2}}(v+H)y^{ab}\bar{D}^{a}_{\alpha}D^{b}_{\alpha} - \frac{1}{\sqrt{2}}(v+H)y'^{ab}\bar{U}^{a}_{\alpha}U^{b}_{\alpha} \\
&- \frac{1}{\sqrt{2}}(v+H)y''^{ab}\bar{L}^{a}L^{b} + \text{ h.c}
\end{aligned} \tag{1.54}$$

where the expression has been rearranged to define Dirac fields in spinor notation,

$$D^{a}_{\alpha} = \begin{pmatrix} d^{a}_{\alpha} \\ \bar{d}^{\dagger a}_{\alpha} \end{pmatrix},\ U^{a}_{\alpha} = \begin{pmatrix} u^{a}_{\alpha} \\ \bar{u}^{\dagger a}_{\alpha} \end{pmatrix},\ L^{a}_{\alpha} = \begin{pmatrix} \ell^{a}_{\alpha} \\ \bar{\ell}^{\dagger a}_{\alpha} \end{pmatrix} \tag{1.55}$$

After diagonalising the three Yukawa matrices, the eigenvalues terms are related to the masses, which can be identified for each generation as,

$$\begin{aligned}
m_{d^i} &= y^{ii}v/\sqrt{2} \\
m_{u^i} &= y'^{ii}v/\sqrt{2} \\
m_{\ell^i} &= y''^{ii}v/\sqrt{2} \\
m_{\nu^i} &= 0
\end{aligned} \tag{1.56}$$

There is a major consequence from the differences between the representation in generation space (Equation 1.52, $SU(2)_L$ doublets), and in mass space, after diagonalising the Yukawa matrices. D^a_α and U^a_α are rotated to diagonalise their corresponding Yukawa matrix, so affected by different transformations. However, the individual $d^{a}_{\alpha\ L}$ and $u^{a}_{\alpha\ L}$ fields are part of the same $SU(2)_L$ doublet. The effect can be seen writing the $W^\pm$ interactions in the mass state representation of the fields which become off-diagonal,

$$\frac{-g}{\sqrt{2}}\begin{pmatrix}\bar{u}_L & \bar{c}_L & \bar{t}_L\end{pmatrix}\gamma^{\mu}W_{\mu}^{+}V_{CKM}\begin{pmatrix}d_L\\ s_L\\ b_L\end{pmatrix} + \text{h.c} \tag{1.57}$$

$$\begin{pmatrix}d'_L\\ s'_L\\ b'_L\end{pmatrix} = V_{CKM}\begin{pmatrix}d_L\\ s_L\\ b_L\end{pmatrix} = \begin{pmatrix}V_{ud} & V_{us} & V_{ub}\\ V_{cd} & V_{cs} & V_{cb}\\ V_{td} & V_{ts} & V_{tb}\end{pmatrix}\begin{pmatrix}d_L\\ s_L\\ b_L\end{pmatrix} \tag{1.58}$$

where the superscript ′ denotes the mass representation and V_{CKM} is the Cabibbo-Kobayashi-Maskawa matrix [29, 30]. This unitary matrix is the product of the transformations that diagonalise the y and y′ Yukawa matrices, which encodes the mixing of the different generations of fields in charged-mediated weak interactions. This is known as flavour violation, where a weak interaction of a quark can result on changing its flavour. On the other side, leptons are represented with the same $SU(2)_L$ doublet, so any mixing of lepton generations is not present in the theory.

feynman diagram?

There is still another interesting feature that arises from the CKM matrix. The standard representation [31] of the matrix takes into account invariant phase rotations of the fields, leaving as free parameters three angles θ_{12}, θ_{23} and θ_{13} (chosen to lie in the first quadrant so $\sin\theta, \cos\theta \geq 0$), and a single complex phase δ that cannot be rotated to zero. The matrix reads,

$$\begin{aligned} V_{CKM} &= \begin{pmatrix}1 & 0 & 0\\ 0 & c_{23} & s_{23}\\ 0 & -s_{23} & c_{23}\end{pmatrix}\begin{pmatrix}c_{13} & 0 & s_{13}e^{-i\delta}\\ 0 & 1 & 0\\ -s_{13}e^{i\delta} & 0 & c_{13}\end{pmatrix}\begin{pmatrix}c_{12} & s_{12} & 0\\ -s_{12} & c_{12} & 0\\ 0 & 0 & 1\end{pmatrix}\\ &= \begin{pmatrix}c_{12}c_{13} & s_{12}c_{13} & s_{13}e^{-i\delta}\\ -s_{12}c_{23} - c_{12}s_{23}s_{13}e^{i\delta} & c_{12}c_{23} - s_{12}s_{23}s_{13}e^{i\delta} & s_{23}c_{13}\\ s_{12}s_{23} - c_{12}c_{23}s_{13}e^{i\delta} & -c_{12}s_{23} - s_{12}c_{23}s_{13}e^{i\delta} & c_{23}c_{13}\end{pmatrix} \end{aligned} \tag{1.59}$$

where $s_{ij} = \sin\theta_{ij}$ and $c_{ij} = \cos\theta_{ij}$. The presence of the complex phase leads to different couplings for anti-matter, as the complex phase will switch sign, thus leading to matter/anti-matter asymmetry. This asymmetry in flavour-changing processes is the only source in the SM of CP violation, or T violation (from the time-reversal symmetry[7]) however, as discussed in Section 1.2.4, fails to describe the current matter/anti-matter content of the universe. The CKM matrix is predicted and measured to be almost diagonal, with very small sources of CP violation, or V_{ub} and V_{td}. The current matrix as in 2022 [16] reads,

$$V_{CKM} = \begin{pmatrix}0.97401 \pm 0.00011 & 0.22650 \pm 0.00048 & 0.00361^{+0.00011}_{-0.00009}\\ 0.22636 \pm 0.00048 & 0.97320 \pm 0.00011 & 0.04053^{+0.00083}_{-0.00061}\\ 0.00854^{+0.00023}_{-0.00016} & 0.03978^{+0.00082}_{-0.00060} & 0.999172^{+0.000024}_{-0.000035}\end{pmatrix} \tag{1.60}$$

[7] The three symmetries are related as the combination, CPT symmetry, which must always be respected in theory.

1.1.6 Flavour Changing Neutral Currents interactions

Flavour Changing Neutral Currents (FCNC) are the processes that involve the change of a fermion flavour through a neutral boson. In the electroweak sector, the neutral current interactions are mediated by the Z boson. Contrary to the $W^{\pm}$ case, the interactions involving the Z boson involve fields with the same associated Yukawa matrix, from the same spinors of the mass representation (Equation 1.55). Hence, no mixing matrix spawns thus are no explicit FCNC appear in the SM Lagrangian.

The existence of charged flavour changing currents is allowed at tree level but their associated couplings are proportional to the off-diagonal elements of the CKM matrix, which are specially small for the interactions between the first and third generation leptons. However, FCNC processes can be obtained from consecutive flavour changing interactions in higher order diagrams. Figure X shows two example FCNC processes involving the two types of first order Feynman diagrams, known as *box* and *penguin* diagrams.

box K->ll and t->c with b and vertices

The high-order contributions are suppresed further by the Glashow, Iliopoulos and Maiani (GIM) mechanism [32]. In order to illustrate this mechanism, the example penguin diagram is discussed in the following. The diagram depicts a top FCNC decay that involves the $t \to b$ and $b \to c$ type of interactions, thus the interaction will be proportional to $V^*_{cb}V_{tb}$. Adding up the other two possible diagrams with d and s in the loop,

$$V^*_{cd}V_{td} + V^*_{cs}V_{ts} + V^*_{cb}V_{tb} \tag{1.61}$$

which assumes that the quarks have the same mass. The value of this expression can be obtained from the CKM matrix. As the matrix is unitary ($V_{CKM}V^{\dagger}_{CKM} = V^{\dagger}_{CKM}V_{CKM} = \mathbb{1}$), a total of 18 constrains appear, relating the different vertices:

$$\begin{aligned}
V^2_{ud}+V^2_{cd}+V^2_{td} &= 1, & V^2_{ud}+V^2_{us}+V^2_{ub} &= 1\\
V^2_{us}+V^2_{cs}+V^2_{ts} &= 1, & V^2_{cd}+V^2_{cs}+V^2_{cb} &= 1\\
V^2_{ub}+V^2_{cb}+V^2_{tb} &= 1, & V^2_{td}+V^2_{ts}+V^2_{tb} &= 1
\end{aligned}$$

$$\begin{aligned}
V^*_{ud}V_{us}+V^*_{cd}V_{cs}+V^*_{td}V_{ts} &= 0, & V^*_{ud}V_{cd}+V^*_{us}V_{cs}+V^*_{ub}V_{cb} &= 0\\
V^*_{ud}V_{ub}+V^*_{cd}V_{cb}+V^*_{td}V_{tb} &= 0, & V^*_{ud}V_{td}+V^*_{us}V_{ts}+V^*_{ub}V_{tb} &= 0\\
V^*_{us}V_{ud}+V^*_{cs}V_{cd}+V^*_{ts}V_{td} &= 0, & V^*_{cd}V_{ud}+V^*_{cs}V_{us}+V^*_{cb}V_{ub} &= 0\\
V^*_{us}V_{ub}+V^*_{cs}V_{cb}+V^*_{ts}V_{tb} &= 0, & V^*_{cd}V_{td}+V^*_{cs}V_{ts}+V^*_{cb}V_{tb} &= 0\\
V^*_{ub}V_{ud}+V^*_{cb}V_{cd}+V^*_{tb}V_{td} &= 0, & V^*_{td}V_{ud}+V^*_{ts}V_{us}+V^*_{tb}V_{ub} &= 0\\
V^*_{ub}V_{us}+V^*_{cb}V_{cs}+V^*_{tb}V_{ts} &= 0, & V^*_{td}V_{cd}+V^*_{ts}V_{cs}+V^*_{tb}V_{cb} &= 0
\end{aligned} \tag{1.62}$$

The equation is exactly one of the constrains, and equals zero. However, as the different quarks are not degerate in mass, every term would be proportional to $1/m_q$ (q being the quark inside the loop). This is the origin of the GIM mechanism and results in a non-zero but very suppressed contribution of FCNC in the SM. In addition, this suppression is larger for loops involving down-type quarks as their masses are more similar than for the up-type quarks.

1.2 Standard Model measurements and top physics

Since the formulation of the SM, most experimental observations and measurements have been described successfully by the model. Throughout the years, predicted particles have been found and multiple precision measurements have tested its validity. However, there are theoretical and experimental issues that are not solved, leading to the conclusion that the SM is an effective theory and there is a more complete theory that can explain the whole range of observations. In this section, a summary of the measurements of the SM is presented, focusing in processes involving the top quar and FCNC. Then, different main open questions of the SM are briefly reviewed.

1.2.1 Experimental measurements

Decades of experiments have performed measurements into parameters that define the SM. The SM can be summarised with nineteen parameters, which have been described in this chapter: nine fermion masses (six for quarks, three for leptons), the three gauge couplings (g_S, g and g'), the Higgs vacuum expectation value (v), the Higgs mass, four parameters of the CKM matrix (three angles and the complex phase) and the QCD CP violating phase. There is no underlying relation between these parameters, only being set from experimental observations. With these parameters measured, theoretical predictions of observables can be tested with experimental data in order to explore new physics.

One typical observable in particle physics is the cross-section σ, the expected interaction rate between two interacting particles in terms of the effective surface area typically measured in *pb* (picobarn, 1pb = 10^{-40} m^2). The cross-section of a process depends on the interacting forces involved, as well as the energy and momentum of the interacting particles, which can be calculated from the S-matrix (scattering matrix) using relativistic mechanics. Feynman diagrams are a tool to translate a visual description of a process to a mathematical expression, the matrix amplitude, which is proportional to the probability of the specific process happening and needed for the computation. The decay width, Γ, can be computed in similar fashion to obtain another common observable, the Branching Ratio (BR). The BR of an unstable particle is the probability for it to decay into specific particles among all possible states. It is computed dividing the Γ of the specific process with respect to the sum of all the possible process. Both σ and Γ are calculated from perturbation approximations, as the actual process is not the product of just one

Feynman diagram, but all the possible interactions that lead to the same final state including loops, interferences and radiative corrections, refereed to as high order corrections. However, each particle interaction is proportional to the probability making higher order corrections become less important. Typically, *leading-order* (LO) calculations use only the leading order terms from the perturbation expansion, while if complemented by higher order corrections are referred to next-to-leading-order (NLO) or next-to-NLO (NNLO) calculations.

Figure 1.3 shows a summary of a wide range of cross-section measurements by the ATLAS Collaboration, compared to the theoretical predictions, showing an excellent agreement between data and theory. In addition, the Higgs boson has been scrutinised since its discovery, to characterise all its properties, unique for its interaction with massive particles. Figure 1.4 shows a summary of Higgs boson production cross-sections and branching ratios by the ATLAS collaboration, including the coupling strengths to other SM particles, showing that the coupling is proportional with the mass of the resulting particle as expected from the Higgs mechanism. As the Higgs couples with any particle that acquires mass through its field, it is an excellent candidate to study any other particle still to be discovered.

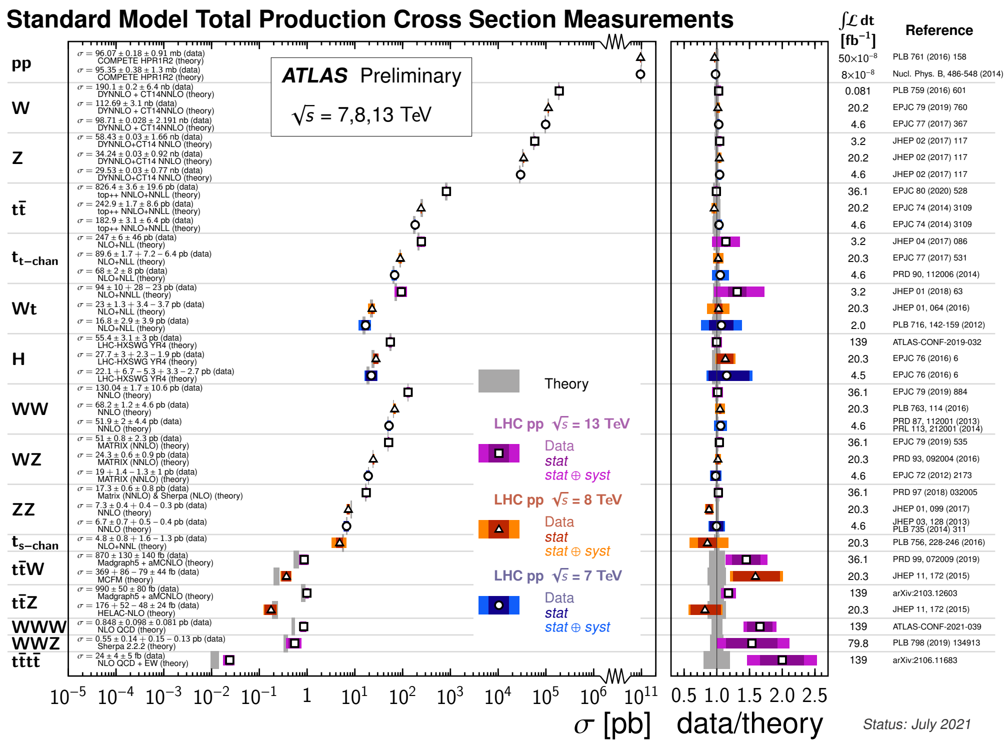

Figure 1.3: Summary of several SM total production cross-section measurements, corrected for branching fractions, compared to the corresponding theoretical predictions and ratio with respect to theory [33].

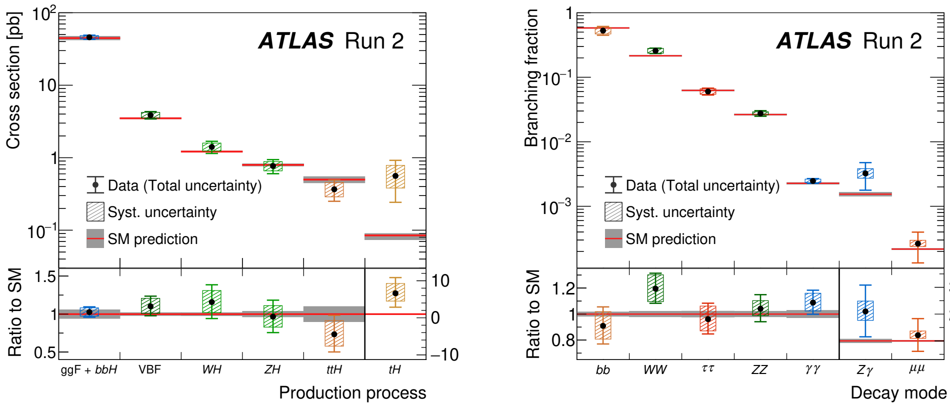

(a) **(b)**

Figure 1.4: Observed and predicted Higgs boson production cross-sections for different production processes (a) and for different decay modes (b). The lower panels show the ratios of the measured values to their SM predictions. The vertical bar on each point denotes the 68% confidence interval. The p-value for compatibility of the measurement and the SM prediction is 65% (a) or 56% (b) [34].

1.2.2 Top quark physics

The top quark is the most massive known elementary particle, discovered in 1995 at Fermilab [11, 12]. Such characteristic makes the top quark the only one that decays before hadronisation and hence, properties like the spin are directly transferred to the decay products. The main top quark decay is $t \to Wb$ with a branching ratio close to 1, determined by the $V_{tb} = 0.97401 \pm 0.00011$ (element of the CKM matrix [16]) being very close to 1. Due to its higgs mass, the top quark strongly couples with the Higgs boson as the Yukawa coupling (Equation 1.56) $y_t = \sqrt{2}m_t/v \simeq 1$.

Altogether, the top quark plays a key role in the study of the SM. The precise measurements of its properties put the theory to test and any deviation would point to new physics. It is also an excellent candidate for searches involving either much more massive particles that might decay to the top quark, or decay into other lighter exotic particles. Even if those new particles are too heavy to be produced at the LHC, they can be targetted by indirect searches and modify the top quark properties.

The top quark can be produced either in top quark pairs, namely $t\bar{t}$ production, or together with other particles, called single-top production. The $t\bar{t}$ production is mainly involves the strong interaction and the main Feynman diagrams are shown in Figure

qq->ttbar, gg->ttbar, crossed, s-channel

The single-top production has three different channels, which involve electroweak interactions: $t-$channel, from W/gluon fusion; $Wt-$channel, with an associated W; and $s-$channel, from $q\bar{q}' \to tb$. Example Feynman diagrams are shown in Figure

qb->q't tchannel, gb->tW Wt, qq'->tb

Figure 1.5 shows a comparison of theoretical and experimental values for the different cross-sections involving the production of different top processes, showing an excelent agreement between them. Also, that the $t\bar{t}$ production is larger than the single-top.

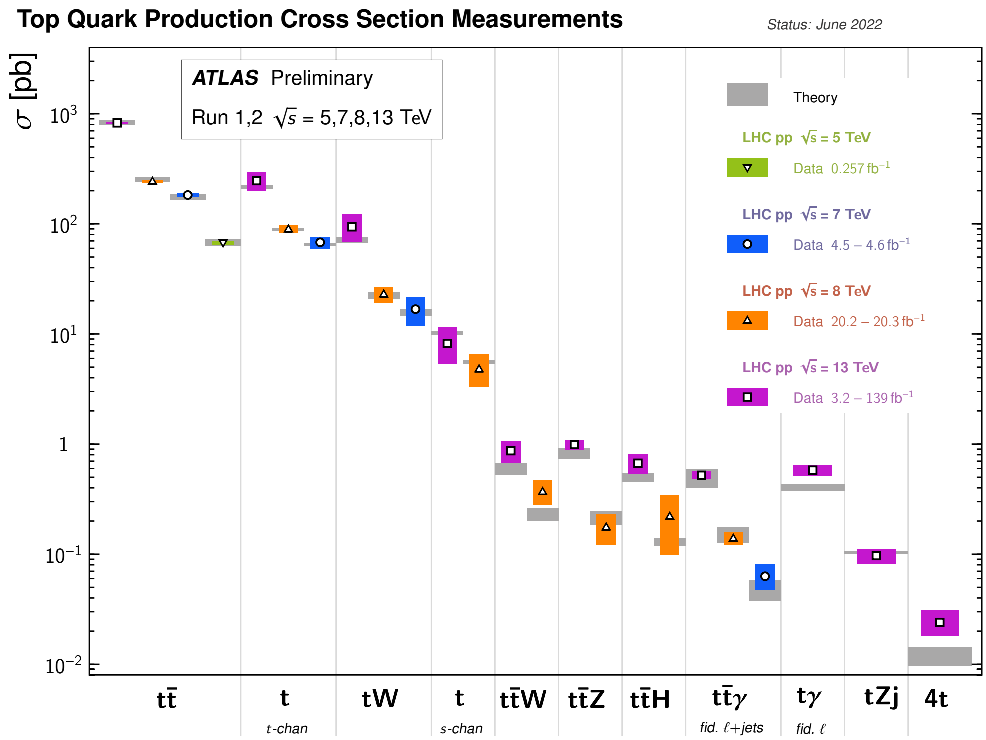

Figure 1.5: Summary of several top-quark related production cross-section measurements, compared to the corresponding theoretical expectations. All theoretical expectations were calculated at NLO or higher [35].

1.2.3 FCNC measurements

A FCNC process stands for an interaction with a change in the fermion (quark or lepton) flavour through the emission or absorption of a neutral boson. As seen in Section 1.1.6, such processes are not allowed at tree-level in the SM and the one-loop contributions are heavily suppresed by the GIM mechanism.

The FCNC interactions involving the top quark are of particular interest, and the possible diagrams are depicted in Figure. As the branching ratio of the top quark is mainly $t \longrightarrow Wb$, together with the heavily suppressed FCNC contributions, the predicted branching ratio for the top FCNC decays in the SM is below $10^{-}14$. This very small value is far away from the achievable sensitivity at the LHC, and makes the precise measurement of FCNC interactions an excelent test of the SM.

depict tgamam uc, tZ uc, tglu uc, tH uc

Table 1.3 shows the SM predictions for all the FCNC top quark decays, together with the experimental results from the SM and CMS collaborations.

Table 1.3: Theoretical predictions for the branching ratios of FCNC top decays predicted with the SM and the most recent experimental limits from the ATLAS and the CMS collaborations.

Process	SM	ATLAS	CMS
$t \longrightarrow u\gamma$	$4 \cdot 10^{-}16$	number ref	number ref
$t \longrightarrow c\gamma$	$5 \cdot 10^{-}14$	number ref	number ref
$t \longrightarrow ug$	$4 \cdot 10^{-}14$	number ref	number ref
$t \longrightarrow cg$	$5 \cdot 10^{-}12$	number ref	number ref
$t \longrightarrow uZ$	$7 \cdot 10^{-}17$	number ref	number ref
$t \longrightarrow cZ$	$1 \cdot 10^{-}14$	number ref	number ref
$t \longrightarrow uH$	$2 \cdot 10^{-}17$	number ref	number ref
$t \longrightarrow cH$	$3 \cdot 10^{-}15$	number ref	number ref

1.2.4 Open questions

Observed neutrino oscillations [36] are only possible if there are mass differences between the three neutrino generations, which implies non-zero masses for some neutrinos although not directly measured. A mass term for neutrinos could be added in the SM in different ways, through adding right-handed neutrinos or as describing neutrinos as Majorana particles [ref]. Nevertheless, the description of the SM particles needs at least seven additional parameters: three for the neutrino masses, three for their mixing angles and one CP violating phase for the neutrino mixing Pontecorvo-Maki-Nakagawa-Sakata (PMNS) matrix [], similar to the CKM quark flavor matrix.

Other measurements that are in tension with the SM predictions are regarding the lepton universality, which is the prediction that charged leptons have identical electroweak interaction strenghts. However, the LHCb collaboration found in 2021 [3] a discrepancy between electrons and muons in decays involving the $b-$quark. An older puzzle is the measurement of the anomalous magnetic dipole momentum of the muon, which was found also in tension with the prediction. This quantity refers to the high order corrections that appear from QCD, and the muon g-2 experiment found a greater deviation [4] in 2021.

The SM also fails to describe the other known fundamental force in nature, gravity. There is no renormalisable QFT for gravity successfully described as general relativity only describes macroscopic systems, with the observation of gravitational waves as a recent achievement[]. There are theories like string theory that provide alternatives although difficult to test experimentally. The SM is understood as an effective theory of a more complete unified theory, hence only valid at low energies and it is expected to break in the most extreme scenario around the Plank scale ($M_P = \sqrt{\hbar/(8\pi G_N)} \sim 2.4\ 10^{18}$ GeV), where gravitational effects are expected to become as important as the other forces in the SM.

The SM describes what is known as baryonic matter, which accounts for about 5% of the energy density of the universe. Cosmology, which studies the composition of the universe, estimates huge amounts of *dark matter* (DM) and *dark energy*, phenomena not contemplated by the SM. The existence of DM was postulated as extra non-luminous matter needed to explain observed rotation curves of galaxies not matching the gravitational pull of observed stars[]. In addition, gravitational lensing effects observed in some galaxy collisions[] also provide the need of huge invisible mass concretations. More recently, the WMAP and Planck collaborations have studied anisotropies in the cosmic microwave background (CMB)[], postulating cold DM. On the other side, the universe is observed to be expanding at an accelerated rate compatible with dark energy, understood to be the product of an intrinsic space-time energy density, or cosmological constant, that causes the expansion. Observation of red-shift of light from supernovae, used as standard candles, points that cosmological objects are moving away at faster rate with the distance[]. Further, studies of the CMB provide another measurements of the accelerated expansion[]. The most updated results[] points that baryonic matter accounts for a mere % of the total energy density of the universe, dark matter for %, while dark energy for %.

The universe seems to be completely made up by matter. To explain the imbalance in abundance of matter and anti-matter, often referred as matter/anti-matter assymetry, the SM only provides one not nearly sufficient source of CP violation in the quark weak interactions. Additional sources are added such as the complex phase in the PMNS matrix, however more phenomena is needed to have generated the current net balance of matter, like possible baryon number violating effects at high energy scales.

Besides the natural phenomena uncovered by the SM, there are also what are known as naturalness problems. Those are aesthetic concerns about the precise different values of some of the SM parameters, which seem "unnatural" if there is no hidden mechanism behind. The general consensus is that the fewer fine tuning is needed in a theory, the more natural it is. Although these matters are completely subjective, these unexplained features could be a hint for the existence of a new underlying mechanism that could complement the SM. The first problem is commonly named as the hierarchy problem, where the cutoff energy of the SM (Λ_{SM}) is commonly set to the Planck scale, $\sim 10^{18}$ GeV, but in contrast the EW scale ($v \sim 246$ GeV) is very small. The problem can be read as there is no apparent reason for the EWSB to happen at its scale, orders of magnitude smaller than the Plank scale. When calculating high-order corrections from the SM, one obtains that the leading radiation corrections for the fermion masses are of the order of $\log \Lambda_{SM}$, sensitive to the scale but the fine-tuning is considered small. On the other side, the physical Higgs mass including radiation corrections reads,

$$m_H^2 = m_0^2 + \frac{3}{8\pi^2 v^2}\Lambda_{SM}^2[m_0^2 + 2m_W^2 + M_Z^2 - 4m_t^2] + \mathcal{O}(\ln\frac{\Lambda_{SM}}{m_0}) \quad (1.63)$$

with m_0 the bare Higgs mass. The nature of the hierarchy problem is evident in the correction as the Higgs mass is more sensitive to the cutoff scale and requires huge tuning to counter the Λ_{SM} term and achieve such a low measured physical mass. It can also be observed that the most important correction is given by the top quark, and it is often questioned whether the reason for the huge mass of this quark could hide a solution. Although the Higgs mass and the EW scale are difficult to justify, it can be argued that the appearance of the Λ_{SM} is related to the chosen regularisation scheme and cut-offs play no physical role.

Another related problem is the fermion mass hierarchy, as the fact that the masses of the SM particles range from $\sim$ 1 MeV to ~173 GeV (of the top quark [16]), it is not understood. Additionally, there is also not an apparent reason for the three mass families of quarks and leptons. It might be related again to renormalisation, since fermion masses also have correction terms with the logarithm of the cut-off scale as stated before.

There is also the problem known as the strong CP problem. The most general QCD Lagrangian could include a CP-violating angle without breaking any symmetry or the renormalisability of the theory. This would lead to the prediction of axion particles and the neutron having non-zero electric dipole moment. Measures of the former in ultracold neutrons and mercury, constrain the CP-violating angle to $|\theta| \lesssim 10^{-10}$[], and supposes an incredibly low value for a parameter that can have any value in the theory.

1.3 Beyond the Standard Model

Intro from Shota

Introduce 2HDM -> potential -> massterms -> H+ FCNC depending on the type Can be part of other theories like SUSY Brief SUSY for hmmsm (what about mh125 models? what are those?)

Charged Higgs phenomenlogy (production and decay)

Flavon -> types of mechanisms -> U(1) (check paper and internal note) Flavon, prediction and decay aswell? assuming f / lambda sm to be cabibo angle 0.23???

The ATLAS experiment at the LHC | 2

The study of particle physics is performed at the TeV scale, in the order of 10^{-15} m, which requires large and complex machines only possible within international collaborations. CERN is one of the biggest and most respected scientific collaborations and, since its origins in the 1950s, has hosted many groundbreaking experiments. The Large Hadron Collider (LHC) [37] is the world's largest particle accelerator, situated underground in the France-Swiss border and in operation since September 2008. The A Toroidal LHC ApparatuS (ATLAS) [38] detector is one of the experiments hosted within the LHC and records the collisions for further data analysis. The work in this thesis is based on the recorded proton-proton collision data at a center-of-mass energy, $\sqrt{s}$, of 13 TeV between 2015 and 2018.

2.1 The LHC

The LHC is a circular particle accelerator with a circumference of 27 km, situated on an average of 100 m underground. The primary activity is the collisions of protons, however proton-Pb and Pb-Pb collisions are also typically performed for one month a year. Particles are steered, collimated and boosted by different types of superconducting magnets and structures along the accelerator ring.

Proton beams circulate over different accelerators before reaching the LHC and the optimal energy. Figure 2.1 shows a schematic view of the CERN accelerator complex. First, protons are extracted from ionised hydrogen and accelerated up to 50 MeV with LINAC2, a linear accelerator. Then, protons are injected into the Proton Synchrotron Booster (PSB), an accelerator made of four synchrotron rings of 157 m in circumference, increasing the energy up to 1.4 GeV. Similarly, the protons are accelerated in sequence to 26 GeV and 450 GeV by the Proton Synchrotron (PS), a circular accelerator of 628 m in circumference, and the Super Proton Synchrotron (SPS), of 6.9 km in circumference. Finally, the protons are injected to the two pipes of the LHC and boosted up to 6.5 TeV before collision. For the Pb operations, the extraction and accelerators prior to the SPS are performed instead using LINAC3 and the Low Energy Ion Ring (LEIR).

Inside the LHC, two particle beams travel close to the speed of light before they are made to collide. The two separated particle beam pipes are designed to operate at 6.5 TeV in opposite directions and kept at ultra-high vacuum, down below 10^{-13} atmospheres. Surrounding the pipes, superconducting magnets built from niobium-titanium alloy coils generate strong magnetic fields of the order of 8 T through an electric current of 11.8 kA. The magnet coils are surrounded by the magnet yoke, tones of solid steel sheets designed to keep the wiring firmly in place and stabilise the temperature of the magnets. The magnets are cooled down to 1.9 K with superfluid helium provided by a cryogenic system requiring 120 tonnes of helium. The rest of external layers is dedicated to shield the particle radiation, insulate the magnet or maintain the vacuum and the whole structure of up to 28

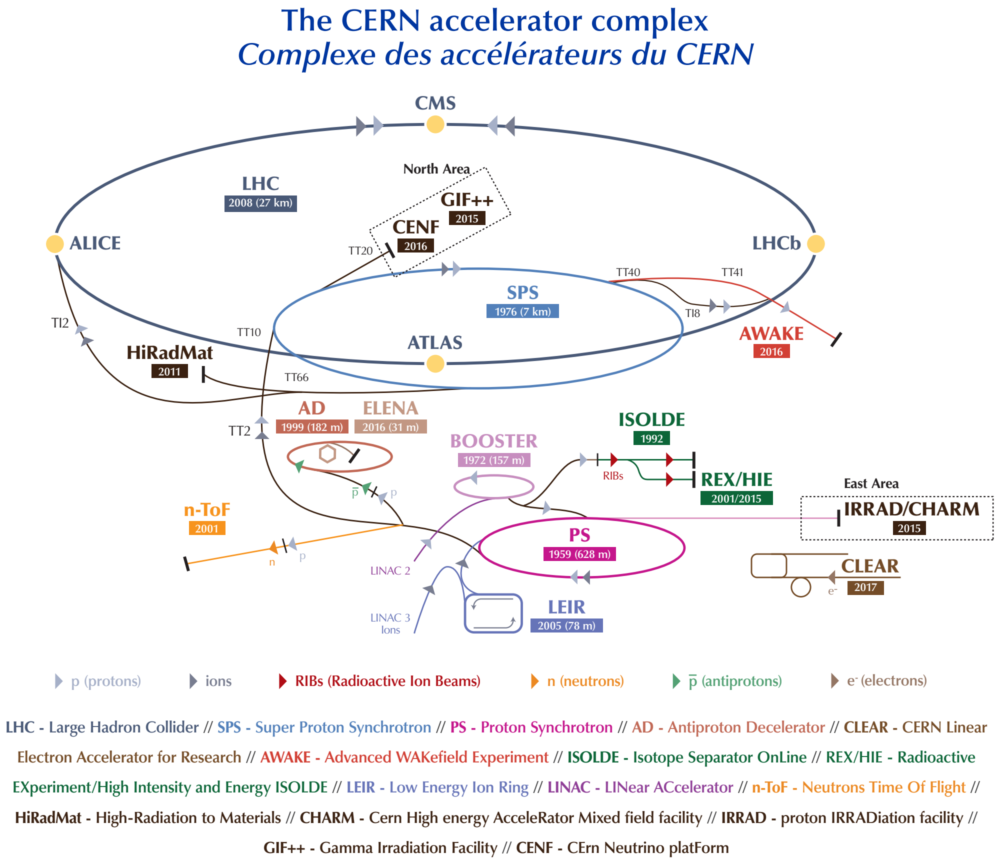

Figure 2.1: Summary of the CERN accelerator complex, with the different accelerators and detectors [39].

tonnes. Different varieties and sizes of magnets constitute the accelerator, mainly 1232 dipole magnets 15 m in length which bend the particle beams to follow the circular trajectory, and 392 quadrupole magnets, each 5-7 m long, which focus the beam. Other types of magnets are used to correct the beam shape or to align them for collision. Figure 2.2 shows the cross-section of a dipole magnet of the LHC, with the different components.

Particles in each beam pipe are accelerated by 8 superconducting radiofrequency (RF) cavities, metallic chambers with alternating electric fields housed in cryogenic chambers, which also space the particles into compact groups named bunches. When protons are accelerated, the bunches contain more than 10^{11} protons spaced every 25 ns (around 7 meters).

The particles are brought to collision at interaction points (IPs) by superconducting multiple magnets focusing the beams. Four detectors are situated at the different IPs: ATLAS, CMS [41], LHCb [42] and ALICE [43]. The first two are multi-purpose experiments that study a wide range of physics, comprising precision measurements of the SM as well as searches for beyond the SM such as Supersymmetry, exotic particles or dark matter. Both collaborations are formed by around 3000 scientists each, the two largest at CERN. The LHCb experiment is dedicated to explore

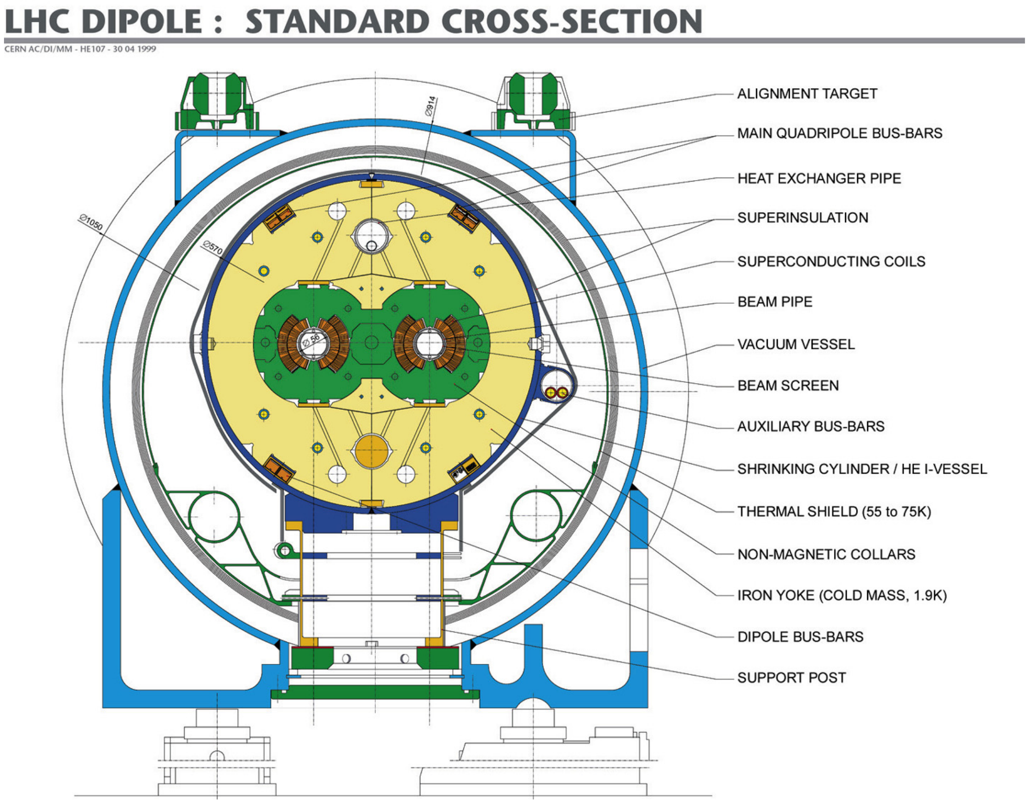

Figure 2.2: Diagram showing the cross-section of an LHC dipole magnet with cold mass and vacuum chamber [40].

hadrons containing b- or c-quarks, especially investigating CP-violating processes. The ALICE experiment is the only experiment fully focused on heavy-ion collisions and therefore specialised on QCD physics.

The Large Electron-Positron Collider (LEP) [44] was the previous main experiment at CERN and its operations finished in 2000 to start the LHC installation in the same tunnel, replacing the predecessor. LEP was designed to collide e^+e^- beams and operated at a maximum of $\sqrt{s} = 209$ GeV. LHC was designed to accelerate protons or lead ions, which in comparison, are easier to accelerate to higher energies and provide more collision data, although harder to be detected and studied. LEP explored the EW scale and provided precision measurements of the SM and set a lower bound for the mass of the Higgs boson, later discovered during LHC operation in 2012. In September 2008, the first LHC operations started and in November 2009 the first collision was produced.

2.1.1 Performance in Run 2

The number of events of a certain process is key for its study and can be written as

$$N = \sigma\mathscr{L} = \sigma \int \mathcal{L} \mathrm{d}t \tag{2.1}$$

where σ is the event cross-section for the given process, $\mathscr{L}$ the integrated luminosity and $\mathcal{L}$ the instantaneous luminosity. The cross-section highly depends on the center-of-mass energy $\sqrt{s}$, one of the main characteristics of a particle collider. As a general rule, the higher the $\sqrt{s}$, the higher is the σ for rare SM processes, interesting for precision measurements or searches for new massive particles.

The instantaneous luminosity is another of the main characteristics of a particle collider, which for the LHC can be approximated [45] to

$$\mathcal{L} = f \frac{n_1 n_2}{4\pi\sigma_x\sigma_y} F \tag{2.2}$$

with f the revolution frequency, $n_{1,2}$ the total number of protons in each beam and F a reducing factor accounting for the beams not colliding exactly head-on and other geometric and beam effects. The first parameter can be approximated to $f = c/27$ km $= 11$ kHz and the total number of protons can be inferred from the nominal number of bunches, 2808, which can contain up to 10^{11} protons. Finally, the denominator is the approximated transverse beam area with transverse beam size $\sigma_{x,y} = 16.6\ \mu$m. With these assumptions, the instantaneous luminosity is of $\mathcal{O}(10^{34}\ \text{cm}^{-2}\text{s}^{-1})$.

During 2010 and 2011, the LHC delivered proton collisions at $\sqrt{s} = 7$ TeV, while in 2012 were at $\sqrt{s} = 8$ TeV. The first proton physics run, namely Run 1, ended in February 2013, which enabled the discovery of the Higgs boson. The evolution of the integrated luminosity delivered of the Run 2 to the ATLAS experiment is shown in Figure 2.3(a) for a total of $\mathscr{L} = 139$ fb^{-1} to be used in physics analysis.

Another parameter of interest is the *pile-up*, which are the additional expected inelastic collisions that occur when crossing bunches of protons. The main source are the collisions that appear within a single bunch crossing, called in-time pile-up. In addition, out-of-time pile-up is referred to interactions from neighbouring bunch crossings not resolved fast enough by the detectors. Pile-up effects are a challenge for physics analysis and is inherent to the increase of instantaneous luminosity. The mean interactions per crossing, $\langle\mu\rangle$, is a measure to quantify the pile-up and has changed throughout the data taking periods, as shown in Figure 2.3(b).

Table 2.1 presents a summary of some LHC operation parameters during Run 1 and Run 2.

Table 2.1: Overview of main operational parameters for Run 1 and Run 2 of the LHC measured by ATLAS [46, 47].

Parameter	2010	2011	2012	2015	2016	2017	2018
Center-of-mass energy [TeV]	7	7	8	13	13	13	13
Integrated luminosity (fb^{-1})	0.47	5.5	23	4.0	38.5	50.2	63.4
Peak luminosity [10^{33}cm^{-2}s^{-1}]	0.2	3.6	7.7	5.0	13.8	20.9	21.0
Av. interactions/crossing	~2	9.1	20.7	13.4	25.1	37.8	36.1
Bunch spacing [ns]	150	50	50	25	25	25	25

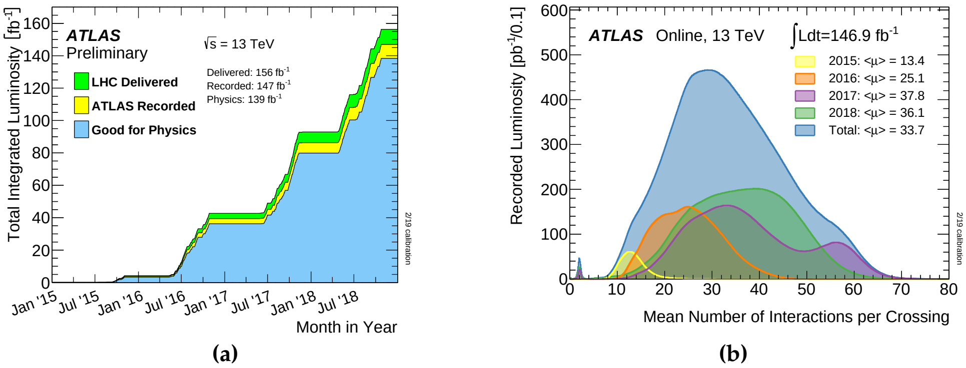

Figure 2.3: The total integrated luminosity delivered by the LHC, recorded by ATLAS and labeled good for physics during Run 2 (a) and the mean number of interactions per bunch crossing splitted into the different data taking periods weighted by the corresponding luminosity (b) [46].

2.2 The ATLAS experiment

The ATLAS detector is a multipurpose particle detector, used to study a wide range of physics topics. It is installed 100 m underground at IP-1 of the LHC. Being 25 m in diameter, 44 m in length and 7000 tonnes in weight, ATLAS is the largest particle detector ever built at a collider. The detecor is illustrated in Figure 2.4, it consists of a cylindrical shape and is composed of several detector layers built around the collision point of the particles, with an almost full solid angle coverage.

The data recorded by the detector is used by the collaboration in an extensive physics program. One of the main branches is the measurement of SM processes, as the large luminosity provided by the LHC allows both precision measurements or to target uncovered phenomena. The data collected during Run 2 allows the study of the Higgs boson and its properties, heavily scrutinised since the first observation of the particle. In addition, measurements of the interactions and processes involving the top-quark are particularly interesting to probe the SM and BSM theories. A large portion is dedicated to a wide range of BSM theories that includes supersymmetry, dark matter or additional resonances among others. Finally, the physics program also includes the study of the physics involving $b-/c-$quarks and heavy ions.

All detector systems are designed such that they provide optimal performance to fulfil the different physics targets. For that, it is important that the detector can identify particles ranging from few GeV to several TeV with outstanding efficiency and resolution, providing accurate measurements of position and momentum. On the other hand, the conditions of the LHC are extreme, and the electronics installed have to be highly resistant to radiation and fast for readout (25 ns between interactions).

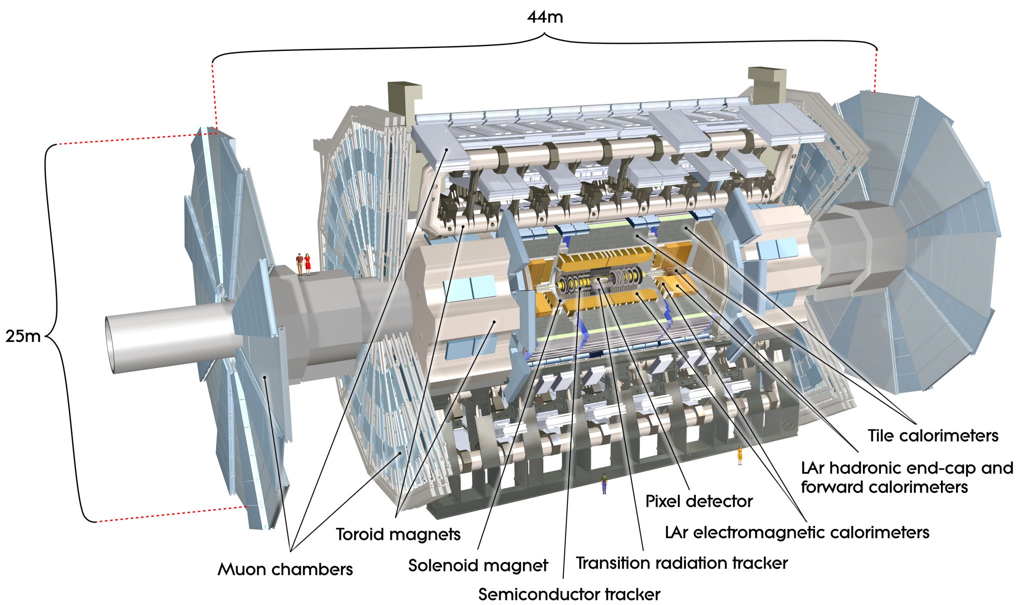

Figure 2.4: Schematic overview of the ATLAS detector [48].

2.2.1 Particle identification

2.2.2 Coordinate System

The convention to describe the particles recorded with the ATLAS detector is a right-handed coordinate system as illustrated in Figure, with the origin at the centre of the detector which is also the interaction point. The z-axis is defined in the counterclockwise direction along the LHC beam line, the y-axis points towards the surface and the x-axis towards the centre of the ring defined by the accelerator. To describe the physics objects within the detector, spherical coordinates are use instead, with the polar angle, θ, measured from the z-axis while the azimuthal angle, ϕ, measured from the x-axis in the $x - y$ plane. The pseudorapidity, η, is usually used instead of the polar angle, as it transforms easily under relativistic boosts along the z-axis. For particles with energy E and forward momentum p_z, the expression of η can be found from the rapidity, y, in the high-energy approximation,

$$y \equiv \frac{1}{2} \ln \left(\frac{E + p_z}{E - p_z} \right) \xrightarrow[\frac{m}{E} \to 0]{} - \ln \left(\tan \frac{\theta}{2} \right) \equiv \eta \tag{2.3}$$

ATLAS covers the pseudorapidity region up to $|\eta| < 4.9$, although physics analyses typically consider objects restricted to $|\eta| < 2.5$. In addition, the difference in η between two points, $\Delta\eta$, is invariant under Lorentz transformation, thus angular distances can be described in the $\eta - \phi$ plane as,

$$\Delta R = \sqrt{(\Delta\eta)^2 + (\Delta\phi)^2} \tag{2.4}$$

Another useful expression is the momentum in the $x - y$ plane,

$$\vec{p_{\mathrm{T}}} = \begin{pmatrix} p_x \\ p_y \end{pmatrix}, p_{\mathrm{T}} = \sqrt{(p_x)^2 + (p_y)^2} \tag{2.5}$$

as at the time of the collision the particles are made to collide along the z-axis, the initial momentum of the transverse plane is known to be zero due to conservation of energy.

2.2.3 The Inner Detector

The Inner Detector (ID) [54, 55] is the innermost detector system, which encloses the beam pipe. This detector system provides precise tracking information of charged particles with momentum as low as 100 MeV with a $|\eta| < 2.5$ coverage. Figure 2.5 shows an overview of the system, which is structured into three sub-detectors: the pixel detector, the semiconductor tracker (SCT) and the transition radiation tracker (TRT).

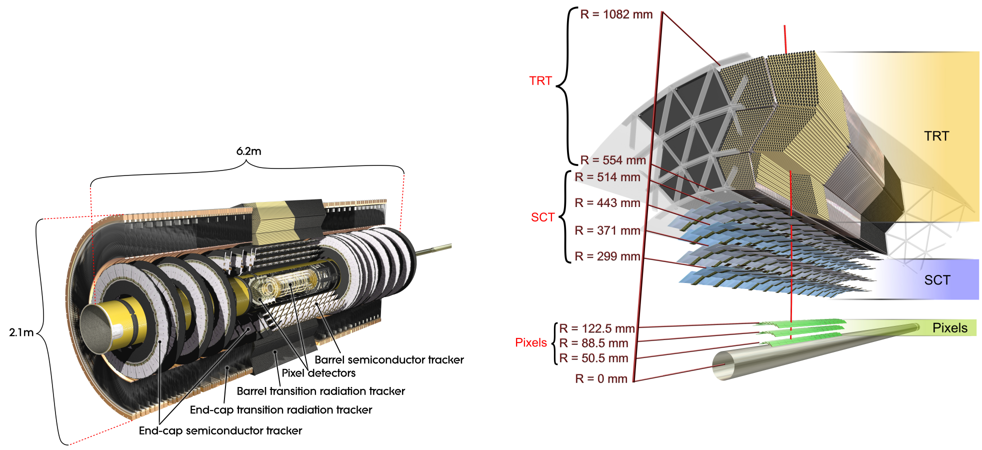

(a) **(b)**

Figure 2.5: Schematic view of the ATLAS Inner Detector (a) and detaileds of the barrel section (b) [48].

Pixel Detector

The inner part of the ID is the silicon pixel detector comprising 4 cylindrical layers and 2 end-caps with 3 disc layers each. The layers are located between 33.25 mm to 122.5 mm around the beam pipe with a coverage of $|\eta| < 2.5$. A single 3D pixel is a radiation-hard silicon detector that produces a small measurable current when a charged particles passes through. The detector is especially important for the reconstruction of tracks, path of charged particles; the primary vertex reconstruction, the position of the main energetic collision; as well as for secondary vertex finding.

The insertable b-layer (IBL) is the innermost layer, installed in-between Run 1 and Run 2, having the highest granularity with a pixel size of 50×250 μm (50 μm in the ϕ-direction and 250 μm in z-direction) for a total of 12 M pixels. In particular, the IBL is very efficient to reconstruct secondary vertices, which are key signatures of long-lived particles decays and crucial for the identification of b-hadrons. Furthermore, the three remaining layers have a pixel size of 50×400 μm. Overall, the pixel detector contains 86 M pixels with an expected hit resolution of 8×40 μm for the IBL and 10×115 μm for the rest of pixel layers. In addition, the system makes up around 50% of all ATLAS readout channels. For the next upgrade, the High Luminosity LHC (HL-LHC), a new fully silicon-based Inner Tracker (ITk) will replace the full ID.

Semiconductor tracker

The semiconductor tracker (SCT) is a silicon strip detector comprising 4 double layers in the barrel region and nine planar end-cap discs on each side, installed around the pixel detector. The planar strips technology is simpler compared to the silicon pixels, for lower resolution covering a larger area. The strips have a size of 80 μm$\times$12 cm and cover a region up to $|\eta| < 2.5$. The two layers within one layer-module are tilted by 40 mrad. Overall, the SCT has a resolution of 17×580 μm with a total of 6.3 M readout channels. In general, the semiconductor-based detectors in ATLAS operate at a temperature between -10 ºC and -5 ºC to suppress different types of electronic noise.

Transition Radiation Tracker

The outermost part of the ID is the transition radiation tracker (TRT). In contrast to the others, the TRT is not based on silicon but is a gaseous detector system. It consists of around 300 k straw tubes with a diameter of 4 mm filled with a gas mixture [1] of Xe (70%), CO_2 (27 %) and O_2 (3 %) and with a gold-plated tungsten wire in the tube centre with a potential different to the tube surface of 1.5 kV. When a charged particle hits the tube, the ionisation of the gas is detected as the signal. The straws have a length of 144 cm in the barrel region and 37 cm in the end cap, while the single hit resolution is 120 μm and 130 μm, respectively. The TRT only provides tracking information in the ϕ direction, as the tubes are parallel to the beamline. Besides, the TRT provides particle identification from emitted transition radiation at the material boundaries, since the straws are interleaved with polypropylene. Especially, electrons can be distinguished from charged pions due to larger transition radiation.

2.2.4 The Calorimeter System

The calorimeter system is responsible for the precise measurement of the energy carried by both charged and neutral particles as well as measuring shower properties

[1] In Run 2, a mixture of Ar (80%) and CO_2 (20%) was used instead in modules with gas leaks

to allow for particle identification. Showers are cascades of secondary particles which are formed when a highly energetic particle interacts with dense material. ATLAS uses sampling calorimeters which consist of alternating layers of active material (liquid argon and plastic scintillators) and passive detector material (copper, iron, tungsten and lead). While the active material measures the energy deposit of the particles going through, the passive material is designed to interact and absorb particles, thus induces the showering. The calorimeter system covers the region $|\eta| < 4.9$ and is places between the central solenoid and the muon spectrometers. Figure 2.6 shows an overview of the system, which is composed of two sub-detectors: the electromagnetic [61, 62] and the hadronic calorimeter [63, 64].

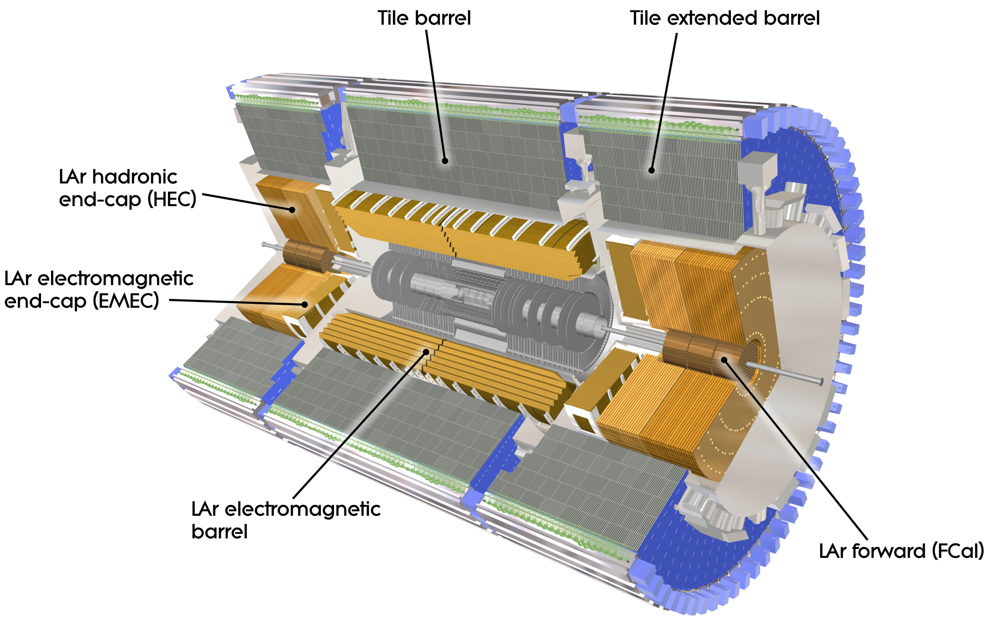

Figure 2.6: Schematic overview of the ATLAS calorimeter system [48].

Electromagnetic Calorimeter

The electromagnetic (EM) calorimeter encloses the ID and is a high granularity calorimeter based on liquid argon (LAr) technology with absorber plates made out of lead. To provide full coverage in ϕ, the EM calorimeter has an accordion-shaped structure where the active material is placed in the gaps between the lead absorber plates and the Kapton electrodes. The detector operates at -183 ºC with a total of 170 k readout channels. The barrel region of the EM calorimeter covers the region $|\eta| < 1.475$ and consists of three layers with a 4 mm gap between them and a length of 3.2 m each, with decreasing granularity. The layer closes to the ID has a granularity of $\Delta\eta \times \Delta\phi = 0.0031 \times 0.098$, while the second layer $\Delta\eta \times \Delta\phi = 0.025 \times 0.025$ and the outermost $\Delta\eta \times \Delta\phi = 0.05 \times 0.025$. In addition, the two end-caps cover the region $|\eta| < 3.2$ with a slightly coarser granularity. In general, the absorption power at high energies of a calorimeter is quantified by means of the radiation length X_0 of its medium. It is defined as the distance over which the particle energy is reduced via radiation losses by a factor $1/e$. The thickness of the barrel region, given in terms of the radiation length, is 22 X_0 and 24 X_0 for the end-caps. Moreover, the intrinsic energy resolution of the EM calorimeter is,

$$\frac{\sigma_E}{E} = \frac{10\%}{\sqrt{E}} \oplus \frac{17\%}{E} \oplus 0.7\% \tag{2.6}$$

Hadronic Calorimeter

The second calorimeter system is the hadronic calorimeter located around the EM calorimeter and consists of three components providing around 19000 readout channels. First, the tile calorimeter is made out of alternating layers of steel as absorber material and scintillator plastic tiles as active material, being read out via photomultiplier tubes. The first two layers have the highest granularity with $\Delta\eta \times \Delta\phi = 0.1 \times 0.1$. The barrel part of the tile calorimeter covers a region with $|\eta|$ < 1.0 and the two extended barrels a range of $0.8 < |\eta| < 1.7$. The resolution of the tile calorimeter is σE/E = 50%/$\sqrt{E}\oplus$ 3% [66, p. 3]. Next, the end-cap calorimeters are directly outside the EM calorimeter and are based on the LAr technology. The end-caps use copper as passive material and cover a region of $1.5 < |\eta| < 3.2$ with their highest granularity of also 0.1×0.1 within $|\eta| < 2.5$. Finally, the forward calorimeter is also LAr based and its first layer uses copper as absorber, which provides information for both electromagnetic and hadronic particles. The other two layers make use of tungsten as absorber which is better suitable for hadronic measurements. In total the forward calorimeter covers a region of $3.2 < |\eta| < 4.9$. The overall resolution of the LAr based hadronic calorimeters is,

check this numbers

$$\frac{\sigma_E}{E} = \frac{50\%}{\sqrt{E}} \oplus \frac{1\%}{E} \oplus 3\% \tag{2.7}$$

σE/E = 100%/$\sqrt{E}\oplus$ 10% [67, p. 2].

2.2.5 Muon Spectrometer

The muon spectrometer (MS) is the outermost detector system of ATLAS, designed to identify and measure the energy of muons. Figure 2.7 shows an overview of the system, which is composed of four detector systems grouped into trigger and precision muon tracking chambers. In total, the MS has more than one million readout channels and is embedded in three superconducting toroidal magnets, that provide a magnetic field in the ϕ-direction. Muons mostly reach the MS without losing energy, and the strong magnetic fields is design for their precise measurement. The p_{T} resolution is around 3% for 10-200 GeV and 10% for 1 TeV muons.

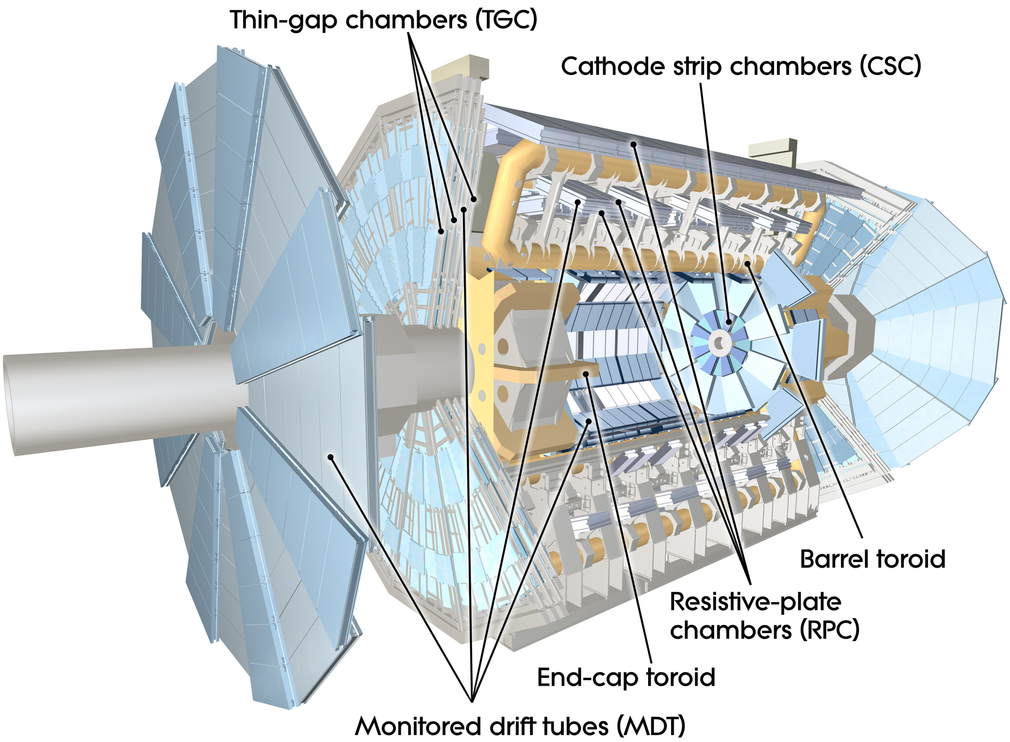

Figure 2.7: Schematic overview of the ATLAS muon spectrometer [48].

Muon Trigger Chambers

The muon trigger chambers are designed for a fast readout to provide energetic muon identification in a timescale compatible with every bunch crossing. In the barrel region, $|\eta| < 1.05$, three layers of resistive plate chambers (RPCs) which consists of two parallel plates with high resistivity and filled with a gas mixture (94.7% $C_2H_2F_4$, 5% Iso-C_4H_{10}, 0.3% SF_6). The RPCs provides an $\eta - \phi$ measurement with a spatial resolution of 10 mm and time resolution of 1.5 ns. thin gap chambers (TGCs) are installed in the end-caps, $1.05 < |\eta| < 2.4$, which are multi-wire chambers filled with a gas mixture (55% CO_2 and 45% n-C_5H_{12}) with the wires separated by 1.8 mm. Besides trigger information, the TGCs provide ϕ information with a resolution of 5 mm.

Precision Muon Tracking Chambers

The precision muon tracking chambers are designed to provide high resolution and precision tracking information, usually after the trigger decision of the trigger muon chambers. The system is mainly composed of monitored drift tubes (MDTs), installed in the barrel and end-cap region covering $|\eta| < 2.7$. MDTs are aluminum drift tubes with 3 cm of diameter filled with a gas mixture (95% Ar and 7%). Each chamber contains 3-8 layers of drift tubes with a spatial resolution of 35 μm. The forward region of the system, $2.0 < |\eta| < 2.7$, is covered by cathod strip chambers (CSCs) and provide a resolution of 40 μm in the radial direction and 5 mm in the ϕ direction. These chambers are proportional multi-wire chambers, similar to the TGCs, with lower response time.

2.2.6 Magnet System

The magnet system is of major importance to allow momenta and charge measurements, bending the trajectory of charged particles depending on these properties. Figure **??** shows an overview of the system, which consists of two sub-systems: the central solenoid magnet, which is located between the ID and the calorimeters, and the toroidal magnet system, embedded within the MS. The solenoid generates a constant magnetic field of 2 T, with a superconducting magnet made out of NbTi cooled via liquid helium to a temperature of 1.8 K. There is one barrel toroid magnet and two end-cap toroid magnets with eight coils each, where each deliver an inhomogeneous magnetic field of roughly 0.5 T and 1 T, respectively.

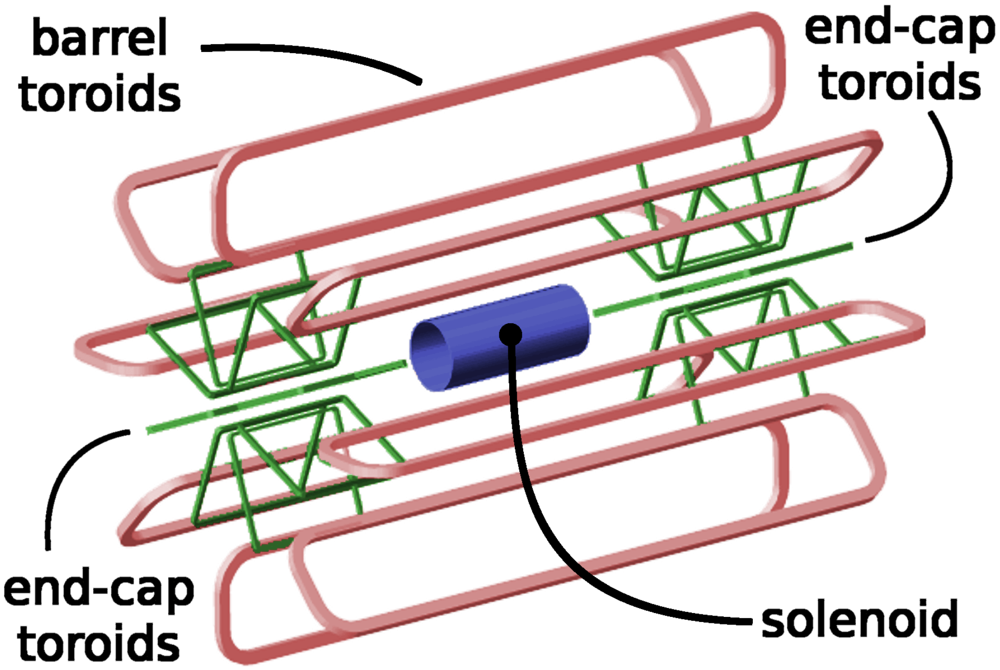

Figure 2.8: Schematic overview of the ATLAS magnet system [49].

2.2.7 Trigger System and Data Acquisition

With a bunch crossing every 25 ns, the LHC produces collisions at a frequency of 40 MHz at nominal operation conditions. For ATLAS is translated to an unmanageable rate of more than 60 TB/s of data. The TDAQ system is designed to select and record the events considered interesting for analysis for an average storage of 1 kHz.

The trigger system, summarised in Figure, is structured into two parts since Run II: the Level-1 (L1) hardware-based trigger system and the software-based high level trigger (HLT). The L1 trigger uses reduced-granularity information from the calorimeters and from the muon RPCs and TGCs to select events with interesting objects (normally high p_{T} electrons, muons, photons, jets or high missing transverse momentum). The latency is of 2.5 μs and reduces the rate from 40 MHz to about 100 kHz, which corresponds to 100 collisions. The information of the collisions is stored in buffers and the Central Trigger Processor (CTP) performs the decision based on the inputs of the other L1 sub-systems. The L1 trigger output are regions of interest (RoIs) in η and ϕ, which are passed to the HLT. The HLT uses the full detector information within the RoIs to reduce the event rate down to approximately 1 kHz with a latency of 200 ms.

After, the data is transferred to a computing centre for further processing and storage. An offline data quality monitoring system performs checks on fully reconstructed events, to ensure their quality for use in physics analyses. Some of the criteria to validate are requirements on the condition and performance of the beams and different ATLAS sub-detectors at the time of operation. As summarised in Figure 2.3(b), from the 156 fb^{-1} of integrated luminosity delivered by the LHC during Run 2, 147 fb^{-1} where recorded by the detector and 139 fb^{-1} cataloged as good-quality data.

Physics simulation of proton collisions 3

Proton collisions are complex processes and their understanding is essential to interpret the experimental data from the LHC. Normally, physics analyses rely on the ability to accurately simulate the various processes of proton-proton collisions and the interactions with the detector in order to perform comparisons with the recorded data and quantify its the level of agreement of the SM. The simulation is usually performed with Monte Carlo Monte Carlo (MC) generators, which are stochastic tools that incorporate both theoretical predictions and empirical results to describe the statistical processes. Sections bla and bla

3.1 Event simulation

The typical proton-proton collision at the LHC is depicted in Figure. The inelastic scattering is the main interesting process, where the energy of the system is large enough so a constituent of each proton (partons) interact and allow the production of additional particles. The interaction that involves any of the other partons, normally at lower energies, is referred to as underlying event. A key phenomenon is the parton shower, a processes where due to the strong interaction, particles loose energy due the radiation of gluons which further generate quark-antiquark pairs, which in turn radiate gluons again in a chain reaction. These generated particles loose energy progressively down to the point where QCD leaves the perturbative regime (~1 GeV) and the hadronisation occurs, when quarks and gluons form hadrons, colorless bound states. To complete the simulation of the collision, the pile-up is included which adds the effects from the other proton collisions that originate from the same or previous bunch-crossing.

3.1.1 Factorisation theorem

The cross-section to produce a final stat X from the hard scattering of two protons, $\sigma_{pp\to X}$ can be factorised into two components in perturbation theory, as the strong coupling constant, α_s, is small at high energy kinematic regimes. Using the factorisation theorem cite,

$$\sigma_{pp\to X} = \sum_{a,b} \int \mathrm{d}x_a \mathrm{d}x_b f_a(x_a, \mu_F^2) f_b(x_b, \mu_F^2) \cdot \hat{\sigma}_{ab\to X}(x_a p_a, x_b p_b, \mu_F^2, \mu_R^2), \tag{3.1}$$

where $f_i(x_i, \mu_F^2)$ are the parton distribution function (PDF) for partons $i = a, b \in \{g, u, \bar{u}, d, ...\}$ and encodes the probability of finding a parton of type i within the proton carrying a fraction of the proton's momentum x_i, at the factorisation scale μ_F. The dependence of the scale appears from performing only fixed-order calculations and the value is typically set comparable to the energy of the process, for example, to the total transverse mass of the final-state particles. The partonic cross-section, $\hat{\sigma}_{ab\to X}(x_a p_a, x_b p_b, \mu_F^2, \mu_R^2)$, is calculated at finite perturbative order, hence the additional dependence on the renormalisation scale, μ_R, at which to evaluate α_s.

3.1.2 Parton density function

The PDFs are crucial for the accurate description of the partons that form the protons. The first type of partons are the valence quarks which determine the quantum numbers of the proton. In addition, gluons and virtual quark-antiquark pairs (sea-quarks) are also part of the proton and come from the vaccum fluctuations. A PDF, $f_i^A(x_i, Q^2)$ describres the probability density of a parton of a certain type, i, inside a given hadron, A to carry a certain momentum fraction, $x = p_i/p_A$ evaluated at a specific momentun transfer Q^2. In general, PDF are excracted from empirical measurements performed at a specific scale. Then, the Dokshitzer-Gribov-Lipatov-Altarelli-Parisi (DGLAP) equations are used to extrapolate the PDF to different scales. Other alternatives to extract the functions like latice QCD are possible, but very computationally challenging. There are dedicated collaborations such as the *NNPDF*, *CTEQ* and *MSTW* that provide PDFs for physics analyses. Figure shows the *NNPDF3.0NLO* PDF set for the different proton partons and two different factorisation scales.

There are two main factorisation schemes to describe processes involving b-quarks: the four-flavour scheme (4FS) and the five-flavour scheme (5FS). The 4FS treats the b-quarks massive ($m_b > \mu_R$) and since $m_b > m_p$, they are not included in the sea of quarks and do not have an associated PDF. In the context of QCD perturbative evolution, one of the consequences is that calculations at lower scales $\mu_R < m_b$ are especially impacted as the α_s running depends on the number of quark flavours in the initial state, $n_f = 4$. On the other hand, at high scales the mass effects are negligible and usually described by the 5FS, in which the b-quark is considered massless, included in the initial state and treated as the other quarks, $n_f = 5$.

reference euqation of the running

3.1.3 Matrix element

The computation of the partonic cross-section of partons i, j into an arbitrary final state X, is related to the ME amplitude as,

$$\hat{\sigma}_{ij\to X} \sim \sum_{k=0}^{\infty} \int \mathrm{d}\Phi_{X+k} \left| \sum_{l=0}^{\infty} M_{X+k}^{l} \right|^2 (\Phi_F, \mu_F, \mu_R) \tag{3.2}$$

were PDFs and other normalisation factors are removed for compactness. M_{X+k}^l is the ME amplitude for the production of X in association with k additional final-state partons, or legs, and with l additional loop corrections. In a perturbative regime, the ME amplitudes for increasingly complex processes (diagrams with additional legs and loops) tend to decrease. As a result, the cross-section is generally computed at a perturbative order, without the sum computed to infinity and for a choice of μ_F and μ_R. The Leading Order (LO) is the lowest possible order for the calculation, with $k = l = 0$. Next, $l = 0, k = n$ provides the LO computation for the production of $X + n$ jets. Finally, $k + l \leq n$ corresponds to a N^{n}LO prediction for the production of X, while also to a N^{n-k}LO prediction for the production of X in association of k jets.

3.1.4 Parton shower

One problem that arises in the fixed order computations of the differential cross-section is the appearance of logarithmic divergences from collinear splitting that originate from the integration of the phase space, Φ, of the additional k partons. For an inclusive cross-section computation, these divergencies cancel out with virtual corrections order by order, following the KLN theorem. In this case, the basic event is simulated at fixed order while the QCD emission process (splitting) is computed with the PS algorithm, which generates a sequence of emissions with decreasing angle or energy. The algorithm recursively produces the typical splitting processes ($g \to q\bar{q}$, $g \to gg$ and $q \to qg$) for each parton until the energy of the shower reaches ~1 GeV, the hadronisation scale. This showering process that is applied to the final products after the hard-scattering is referred to as final state radiation (FSR), while the simulation of the inistial state radiation (ISR) is performed to the incoming partons. In the case of ISR, the subsequent emissions grow on energy and are modelled instead with a backwards-evolution algorithm.

There is an incompatibility with ME and PS for a full cross-section computation at order $n > 1$, as there is a possible overlap in the phase space of the extra partons that are considered for the ME at order n with the ones considered in the splitting at order $n - 1$. There are different approaches to solve the double counting, known as ME-PS matching. The most common strategy is known as slicing, which defines a matching scale where the higher energy region is covered only by the ME while any additional parton with energy below the scale is vetoed and only covered with the PS algorithm. With this strategy, both energy regions are described with the corresponding optimal algorithm.

3.1.5 Hadronisation

The hadronisation process starts when the energy of the PS emissions is low enough to reach the hadronisation scale (~1 GeV), where the perturbative regime of QCD is not valid. At that point, the partons from the PS have defined momentum, flavour and color and furhter description of the emissions has to rely on phenomenological models. The process consists on a reconstruction algorithm that groups together the partons into different hadrons, that can further split, until all partons are confinend into stable hadrons.

The two most widely used models are: the Lund string model and the cluster model. In the first, the quark-antiquark pair colour interaction is described as a string with a potential assumed to be linearly increasing with the distance, emulating the

QCD potential. The string then splits forming new quark-antiquark pairs when the energy stored passes the quark-antiquark total mass, forming hadrons which momentum is determined from the initial momentum by a fragmentation function. The momentum of the hadron as a fraction . On the otherhand, the second model is based on forcing the final state gluons to split into quark-antiquark pairs and then grouping all quarks in colour-singlet clusters, allowed to decay and split into smaller clusters or hadrons. For both models, the process is repeated iteratively until only stable hadrons remain.

3.1.6 Pile-up and underlying event

Other interactions aside the hard-scattering event have to be included in the MC simulations to properly model the LHC collisions, the pile-up and the underlying event. Both sources mainly consist of soft QCD interactions, the first arising from other protons colliding in the same or previous bunch-crossing while the second being the interaction of the other partons that do not originate the hard-scattering process. Both mainly consist of soft QCD interactions in the forward regime, close to the beam axis, and the description is based of the combination of phenomenological models and the configuration of the LHC beam. In the especial case of out-of-time pileup (interactions from previous bunch-crossings), the simulation has to take into account the time response of the detector.

3.1.7 Monte Carlo simulation and generators

MC generators are dedicated software tools to perform the MC simulations, based on pseudo-ranom numbers to generate the events from the predicted distributions. They are generally classified according to which of the steps of the simulation can perform, with general purpose generators being capable of simulating the whole event process, while dedicated generators target specific parts of the chain, such as the ME or the PS computation.

The full process involving ME generation, PS, underlying event, hadronisation and fragmentation can be simulated by MC generators like Pythia 8 , Herwig 7 or Sherpa. However, Pythia 8 provides leading order calculations which are often not sufficient and hence, the generator is tipically used to compute the PS process, which is based on the Lund string model. On the other hand, Herwig 7 provides many ME at NLO, however since the fraction of negative event weights can be quite large (up to $\sim 40\%$ for certain generator setups), the generator is also tipically used for PS computation, based on the cluster model. Powheg-Box and MadGraph5_aMC@NLO are examples of other generators that are especially designed to provide accurate high-order ME calculations which are typically interfaced with Pythia 8 or Herwig 7 for the simulation of PS and hadronisation.

More in detail, these tools have parameters to describe the non-perturbative processes that can be tuned using collision data. The most common tunes used by the ATLAS collaboration are the A14 parameters combined with *NNPDF3.0LO* PDFs set for Pythia 8 and the H7UE set with the *MMHT2014LO* PDFs sets for Herwig 7.

Throughout this thesis different combinations of MC generators and settings, which are detailed in the corresponding chapters and, if not stated otherwise, share the same parameters. The mass of the top quark is set to $m_t = 172.5$ GeV, the mass of the Higgs boson to $m_H = 125$ GeV and the mass of the b-quark to $m_b = 4.8$ GeV for Pythia 8, to $m_b = 4.5$ GeV for Herwig 7 and to $m_b = 4.75$ GeV for Sherpa. The simulation involving b- and c-hadron decays is performed with EvtGen (except for Sherpa).

3.2 Detector simulation

With the proton-proton collisions simulated and the final-state stable particles defined, the remaining step is to simulate the interactions with the detector. The full ATLAS detector simulation is performed in two steps: first, the ATLAS detector response of the MC output is simulated and then the signals are reconstructed using the same algorithms used in real data. Figure depicts the different steps both for data and simulated MC events.

The Geant 4 package is a widely used in physics to simulate the propagation and interaction of particles with matter. The simulation that includes all the geometry of the ATLAS sub-detector systems with Geant 4 is referred to *Full Simulation* (FullSim), which is computationally expensive (several minutes per event) but gives the most accurate result. As more than 90% of the dedicated CPU time is spent on the calorimeter simulations, alternatives are used in practice. The *AtlFast-II* (AF-II) simulation is performed with faster simulation algorithms for the calorimeter simulation, ATLAS Fast Calorimeter Simulation (FastCaloSim) , and for the ID simulation, Fast ATLAS Tracking Simulation (Fatras) . The rest of systems are simulated with Geant 4 adding to significantly less CPU time while maintaining an adequate level of accuary. Finally, the normalisation of a SM process is normally chosen according to the cross-section at the highest-order available and other corrections are applied in the form of scale factors (SFs), derived from the ratio between data and MC in specific calibration regions.

Object reconstruction 4

The concept of *reconstruction* refers to the use of algorithms for the identification of physics objects from the signals recorded in the different sub-systems of the detector. The physics processes described in this thesis produce electrons, muons, taus, photons, neutrinos and quarks in the final state. However, not all of these listed particles can be directly observed, as quarks form cascades of hadronic particles, neutrinos leave without interacting with ATLAS and tau leptons decay before reaching the detector. Figure illustrates the interaction of different particles with the ATLAS detector. Charged particles produce a track in the ID, electrons and photons shower in the EM calorimeter, hadrons shower in the hadronic calorimeter and muons leave signals in the muon spectrometer.

The reconstruction of the different physics objects used in this thesis analyses is described in the following chapter.

4.1 Base objects

The fundamental blocks used in the reconstruction algorithms are tracks, vertices and topo-clusters (or calorimeter energy clusters). All physics objects are composed by these blocks and introduced in the following section.

4.1.1 Tracks and vertices

Tracks are objects produced by charged particles interacting in the ID and used to identify their trajectory. The reconstruction consists in grouping hits in the different tracking sub-systems and requiring different criteria to ensure the quality of the tracks. The tracks that originate from the hard-scattering are referred to as primary tracks, and the origin of the track (vertex) is referred to as the primary vertex (PV) (PV)

As a first step, hits are built from groups of pixels and strips that reach a threshold energy deposit starting from the inner layers ID. The seed to reconstruct a track consists in three hits in the silicon detector, and then hits from the outer layers of the tracker compatible with the trajectory are added iteratively. When adding points, a score is assigned to the track to quantify the correctness of the track trajectory and suppresses the contribution of random collections of hits (or fake tracks). Then, a dedicated algorithm evaluates the different seeds to limit shared hits, which typically indicate wrong assignments. In addition, quality criteria are applied where tracks are required to have $p_{\mathrm{T}} > 500$ MeV, $|\eta| < 2.5$, minimum of seven pixel and SCT clusters, a maximum of either one shared pixel cluster or two SCT on the same layer, no more than one missing expected hit (or hole) in the pixel detector and a maximum of two holes in both pixel and SCT. Also, requirements in the transverse impact parameter calculated with respect to the beam position,

$|d_0| < 2$ mm, and related to z_0, the longitudinal difference between the PV and d_0 along the beam, $|z_0 \sin\theta| < 3$ mm. As a last step, TRT hits are added to the tracks after extrapolation.

Vertices are of particular interest as they are the origin of the charged particles or interactions. The PV is the most important, as denotes the origin of the hard-scattering interaction, but secondary vertices are also characteristic of long-lived particles or for heavy-flavour tagging. not talked yet

For a given event, the PVs are reconstructed iteratively from tracks using a dedicated vertex finding algorithm. From a set of quality tracks, a candidate position is defined and the compatibility with the set of tracks in terms of weights is evaluated in order to recompute the vertex position. In each step then, the tracks that are less compatible are given smaller weights and, after the convergence of the optimal vertex position, are left unassigned and remain as input for the following vertex. The PV is defined as the vertex with the largest p_{T}^2 sum.

4.1.2 Topological clusters

Topological cell clusters, or topo-clusters, are objects reconstructed iteratively from calorimeter information and are the first step in the reconstruction of electrons, photons and hadrons. The seed consists of calorimeter cells which readout signal is four times higher than the background noise, and neighbour cells are added if the ratio is higher than two. As a last step, an extra layer is added regardless of the signal-to-background ratio. a little bit weak?

4.2 Jets

Jets are the cone-shaped collimated showers formed by the hadronic cascades that originate from the complex interactions of quarks and gluons when travelling through the detector. These objects are essential for physics analyses with partons in the final state, especially b-quarks, which jets have particular properties that can be used to characterise them with great efficiency. Nevertheless, the kinematic properties of the cascades are challenging to define, as they can contain information from one or multiple final state partons and from the hard-scattering or other radiation processes. There are different possible definitions that depend of dedicated algorithms which group calorimeter information and do not depend on common QCD effects. Jet algorithms are collinear safe, referred to the jet not changing if two constituents are merged forming one with double the momentum (or vice-versa), and infrared safe, meaning that the reconstruction is not affected by adding low p_{T} particles.

4.2.1 Reconstruction

The jet reconstruction is typically performed using the anti-k$_t$ algorithm. . This family of algorithms merges clusters based on a relative distance defined as,

$$d_{i,j} = \min(p_{\mathrm{T},i}^{2n}, p_{\mathrm{T},j}^{2n})\frac{\Delta R_{i,j}}{R^2} \tag{4.1}$$

with $p_{\mathrm{T},i/j}$ the p_{T} of the cluster i and j, $\Delta R_{i,j}$ the angle separation between them, R the chosen radius parameter that sets the size of the jet and n chosen integer that defines the p_{T} dependance of $d_{i,j}$. The decision to combine clusters or to define a cluster as a jet comes from comparing the $d_{i,j}$ value with the beamspot distance, $d_{i,B} = p_{\mathrm{T},i}^{2n}$. Clusters are grouped if $d_{i,j} < d_{i,B}$, otherwise the cluster i is defined as a jet, in an iterative process until all input clusters are used. The anti-k$_t$ algorithm is defined by setting $n = -1$, which groups with higher priority the high energy clusters, and leads to a cone-shape around the highest object. This feature can be observed in Figure.

Various jet collections based on the anti-k$_t$ algorithm are used in ATLAS, two of them are used in this thesis: EMTopo jets and Pflow jets.

EMTopo jets

The so-called EMTopo jets were the primary jet collection used in physics analyses in ATLAS before the end of Run 2. The reconstruction is performed at the EM energy scale only using topo clusters with the anti-k$_t$ algorithm implemented in the *FASTJET* software package . The jets used in this thesis are reconstructed with the radius parameter $R = 0.4$ with requirements in $p_{\mathrm{T}} > 25$ GeV and $|\eta| < 2.5$. The EMtopo jets are calibrated in several steps summarised in Figure . After the jet reconstruction, the jet direction is modified such that the jet originates from the primary vertex. Then, energy corrections based on pile-up are applied subtracting the average energy due to in-time pile-up and other residual corrections that depend on the number of PV and bunch crossings. After, absolute calibrations are applied to the jet energy scale JES and η derived from dedicated dijet MC events. Then, a global sequential calibration is set to improve the p_{T} resolution and the associated uncertainties from the jet fluctuations that can arise from various initial factors like the flavour or energy of the original parton. The final step is the in-situ calibration which is only applied to data, extracted from p_{T} and η comparisons to known well-modelled MC that include central jets in dijet events, $\gamma/Z + jets$ or multijet events.

PFlow jets

Particle Flow jets, known as PFlow jets, were introduced during Run 2 and combine tracking and calorimeter information. This collection of jets has improved energy and angular resolution compared to EMTopo jets and enhanced reconstruction and stability against pile-up. The reconstruction is also based on the anti-k$_t$ algorithm with $R = 0.4$, and the first step consists in matching the tracks (from the ID) from charged particles to the topo-clusters. The energy deposits of the matched topo-clusters are replaced by the corresponding track momentum. Then, the resulting topo-clusters and the tracks matched to the PV are used as input of the anti-k$_t$ algorithm. The jets are calibrated like the EMTopo jets in the range 20 GeV $< p_\mathrm{T} <$ 1500 GeV.

4.2.2 Jet tagging

Jet or flavour tagging consists in identifying the parton flavour that generated the signal reconstructed as the jet. Efficient tagging is essential for analyses studying processes with b- or c-quarks in their final state (knows as heavy flavour quarks), as it is additional information which can be used to select events based on the flavour of their jets and improve the selection of the signal.

Jets originating from the hadronisation of b-quarks, or b-tagged jets, leave a distinct signal due to the properties of b-hadrons: lifetime of $\sim 10^{-}12$ s (decay after 2.5 mm with a momentum of 30 GeV), mass of $\sim$ 5 GeV and high decay multiplicity (including semi-leptonic decays). Figure shows a scheme of a typical signal, that includes displaced tracks from the PV with large d_0. The signal of the c-hadrons is similar but not identical as the lifetime, mass and decay multiplicity are lower, which makes the distinction between these two kinds of jets difficult. The last type of jet is referred to light-flavour jets, which signal originates directly from quark fragmentation and can be easily separated from b-jets. However, other phenomena like long-lived particles, photon conversion or low quality tracks can also prompt displaced vertices and tracks.

Algorithms

Flavour tagging algorithms use the properties of a given jet to return a score, referred to as output discriminant, which indicates how likely the input jet is considered to be a b-, c- or $light$-jet. Two main taggers are used in ATLAS: the MV2c10 tagger which was the default option for EMTopo jets, and the DL1r tagger that is the recommendation for PFlow jets.

The MV2c10 tagger is based on the MV2 algorithm, which relies on boosted decision trees (BDTs) trained with several kinematic and other trigger taggers as inputs. This particular tagger was trained with $t\bar{t}$ and Z' events, to cover a large p_T spectrum, and b-jets defined as signal while the background was defined to consist of 7% c-jets and 93% light-jets.

The DL1r tagger is a multi-class Deep Neural Network (DNN) model, with three output nodes corresponding to the classification of the input jet to be a b-, c- or light jet. The final discriminant is given as a function of the three probabilities. The input consists in the MV2c10 tagger input, additional variables for c-jet identification used in a jet vertex finder algorithm and flavour probabilities provided by a recursive NN . The training set consists of the same $t\bar{t} + Z'$ events, weighted to have an equal mix of quark flavour jets. NN defined at this point?

Comparing the two algorithms used in this thesis, the DL1r tagger is the most recent recommendation and relies on more advanced machine learning techniques than the MV2c10 tagger. The multi-class output together with the possibility of tunning the final discriminant computation, makes the DL1r tagger more flexible than the binary classification of the MV2c10. Regarding performance, the efficiency of both algorithms to tag true b-jets is comparable, while the rejection rates of c- and light jets is greater for the DL1r tagger. The improvement in rejection for the 60% WP, detailed below, is by up to 70% for c-jets and 120% for light jets.

Working points

The full spectrum of the final b-tagging discriminant is not directly used in physics analyses due to the complexity of the calibration. Instead, four different b-tagging working points (WP) are defined based on the b-jet acceptance efficiency evaluated on a $t\bar{t}$ sample: 60%, 70%, 77% and 85%, which are often referred to as *Very Tight*, *Tight*, *Medium* and *Loose* operating points, respectively. Most of the c- and light-jets do not pass the 85% WP, ending up in the b-tagging efficiency between 85% and 100%. Meanwhile, the jets that pass the 60% WP mainly consists in b-jets. This criteria is important when defining the b-jets for event selection, as the $b-$jets misidentification, so c- and $light$-jet acceptance inefficiency, improves for lower b-jet efficiency working points, therefore rejecting more background but with lower signal statistics. On the other hand, the pseudo-continuous b-tagging WP, so the WP that a jet passes, is additional information that can be used to further refine the selection or in multivariate methods.

4.3 Leptons

4.3.1 Electrons

Electrons interact with the ID and the EM calorimeter system. The typical signature is a track in the ID and electromagnetic shower in the EM calorimeter. Overall, the performance in terms of identification and reconstruction of electrons is high.

First, topo-clusters are selected and matched to ID tracks in the region $|\eta| < 2.47$ excluding the transition region of the barrel and end-cap ($1.37 < |\eta| < 1.52$). Next, the matched clusters are grouped to form superclusters, which are variable-size clusters, using a dynamic clustering algorithm. After a first energy and position calibration, tracks are matched to the electron superclusters. The calibration of the energy scale and resolution of electrons is computed from $Z \to ee$ decays and validated in $Z \to \ell\ell\gamma$. In addition, the energy resolution of the reconstructed electron is optimised using a multivariate algorithm based on the properties of showers in the EM calorimeter.

Further identification criteria are required for an electron candidate, passing a selection to increase the purity. The prompt electrons are evaluated with a likelihood discriminant to define three operating points with different purities: *Tight*, *Medium* and *Loose*. The discriminant is computed using variables measured in the ID and the EM calorimeter, chosen such that they discriminate prompt isolated electrons from other signals deposits (jets, converted photons or other electrons from heavy-flavoured hadron decays). The most important quantities are based on the track quality, the lateral and longitudinal development of the electromagnetic shower as well as the particle identification in the TRT. The probability density function to build the likelihood are derived from $Z \rightarrow ee$ ($E^{\mathrm{T}} > 15$ GeV) and $J/\psi \rightarrow ee$ ($E^{\mathrm{T}} <$ 15 GeV) events.

Another requirement is the isolation criteria, to require the electron signal to be separated from other particles. Electrons are typically required to be spatially separated from other particles, based on two quantities: a maximum value for the sum of transverse energy of topo-clusters in a $\Delta R = 0.2$ cone surrounding the electron and of the sum of transverse momentum of tracks around the electron, with a ΔR cone that decreases with p_{T}. Effects of leakage and pile-up are taken into account and also tracks are required to satisfy $p_{\mathrm{T}} > 1$ GeV, $|\eta| < 2.5$ and quality criteria. In this thesis, the criteria used is the Gradient isolation which has an efficiency of 90% at $p_{\mathrm{T}} = 25$ GeV and 99% at $p_{\mathrm{T}} = 60$ GeV.

4.3.2 Muons

Muons leave the ATLAS detector without significant energy loss. The typical signal consists on a track in the ID and MS sub-detectors. There are different types of muons depending on which ID, MS or calorimeter information is available .

As a summary, the muon reconstruction has two stages: tracks are reconstructed independently in the ID and MS, and then are combined to form the muon tracks. The muon track candidates are built from track segments found in the different MS sub-systems. In the muon trigger chambers and MDTss, segments are reconstructed with a straight line to fit the hits of each detector layer after an alignment to the trajectory in the bending plane of the detector. The RPCs, TGCs and CSCs hits provide measurements in the orthogonal direction and the forward region of the detector to build additional track segments. The muon track candidates are then built from the track segments fit together using a global χ^2 fit. With that information, different types of muons can be defined.

The combined (CB) muons are the muon candidates obtained from using combined information from MS tracks that are extrapolated to the tracks of ID (an inside-out approach is also used). The segment-tagged (ST) muons are reconstructed from tracks in the ID extrapolated to typically one track segment in the MDTss and CSCs. ST muons are normally low in p_{T} and in regions with low acceptance. Calorimeter-tagged (CT) muons are built from an ID track that is instead matched to an energy deposit in the calorimeter compatible with a minimal ionising particle. The CT muon strategy outputs the lowest purity, although proves useful for detector regions not fully covered by MS, optimised for 15 GeV $< p_{\mathrm{T}} <$ 100 GeV and $|\eta| < 0.1$ is optimised. The fourth type, extrapolated (ME) muons, are only reconstructed using the MS with an acceptance of $2.5 < |\eta| < 2.7$.

The muon identification criteria (similar to the electron identification) is performed applying quality criteria to increase the purity of the selection. In order to identify prompt muons with high efficiency and a good momentum resolution, a requirement is done for amount of hits in the ID and the MS systems. Four different muon operating points are defined: *Tight*, *Medium*, *Loose*, *high* p_T and *low* p_T. The Medium and Loose working points are used in this thesis. The first one is widely used in physics analyses and is designed to minimise muon reconstruction and calibration systematic uncertainties. It consists of combined and extrapolated muons with three or more hits in at least two MDTs layers, or just one hit for $|\eta| < 0.1$ with no more than one hole in the MS. On the other hand, the Loose working point maximises the reconstruction efficiency and accounts all types of muons, adding the segmented- and calorimeter-tagged muons for $|\eta| < 0.1$. The reconstruction efficiency for muons with $p_{\mathrm{T}} > 20$ GeV at the Medium and Loose working points is 96.1% and 98.1%, respectively. beginning

The isolation criteria is based on track and calorimeter variables, similar to the electron case. The criteria improves the efficiency removing non-prompt muons, the ones not generated in the hard-scattering but in other parton shower processes for example, which are usually close to jets and other objects. The track related variable, $p_{\mathrm{T}}{}^{\mathrm{varcone30}}$ is the scalar p_{T} sum of the additional tracks in a cone $\Delta R = 10\ \mathrm{GeV}/p_{\mathrm{T}}^{\mu}$ (maximum of 0.3), that depends on the muon transverse momentum $p_{\mathrm{T}}{}^{\mu}$. The calorimeter related variable is the same as for electrons, build from the sum of energies around the muon track. In this thesis, the *FixedCutTightTrackOnly* working point is used, which is defined only with track isolation: $p_{\mathrm{T}}^{\mathrm{varcone30}}/p_{\mathrm{T}}^{\mu} < 0.06$.

4.4 Taus

The τ leptons typically decay before reaching active electronics of the ATLAS detector and have to be identified via their decay products. The decay can be either leptonically (into electrons or muons) or hadronically. The leptonic decay represents the 35% of the cases and is covered by the reconstruction of the produced electron or muon. The hadronic decays represent 65%, which contain one or three charged pions in 72% and 22% of the cases, respectively. In addition, at least one associated neutral pion is also produced in 68% of the hadronic decays. The dedicated τ reconstruction and identification algorithms in ATLAS target the hadronic decay, with the main background being jets from energetic hadrons produced in the fragmentation of quarks and gluons, known as the QCD background. Therefore, the τ objects in ATLAS mentioned in this thesis refer to hadronically decaying τ leptons.

The candidates are seeded by jets which are required to have $p_{\mathrm{T}} > 10$ GeV and $|\eta| < 2.5$ excluding the barrel-end-cap transition region . The tau identification is based on a machine learning classifier which is trained using the calorimeter information and the tracks associated to the jet candidate. A trained BDT is used for EMTopo jets while a recurrent neural network (RNN) is used for PFlow jets. Three different efficiency working points are defined: *Loose* , *Medium* and *Tight*. The τ leptons used in this thesis are defined with the medium working point, required to have $p_{\mathrm{T}} > 25$ GeV and an isolation criteria of $\Delta R < 0.2$ between the τ and any selected electron or muon.

4.5 Missing transverse energy

The missing transverse momentum, also denoted as $\mathrm{E}_{\mathrm{T}}^{\mathrm{miss}}$ is the transverse component of the negative vector sum of the fully calibrated objects (electrons, muons, photons, τ leptons and jets) as well as soft objects associated to the PV. In an ideal detector, the the sum of four-momenta of all particles produced is equal to the net momentum of the initial collision, implying that the net momentum in the transverse plane of the collision has to be zero, $E_{\mathrm{T}}^{\mathrm{miss}} = 0$. Nevertheless, the net momentum is not null as particles like neutrinos leave the detector without depositing energy or others can interact with the detector in regions not covered by electronics. For analyses with neutrinos in the final state, it typical to consider that the transverse energy carried by the neutrinos is the $E_{\mathrm{T}}^{\mathrm{miss}}$, which allows their reconstruction.

Machine learning 5

Machine Learning (MC) is one of the core developing fields in computer science allowing the analysis of large and complex datasets, offering sophisticated techniques with a broad range of possible applications. Regarding high energy physics, the large amount of MC simulations or data that is being recorded is well suited for the application of ML techniques.

The deployment of these methods is already reaching crucial tasks as online data recording in ATLAS, from neural networks in calorimetry FPGAs to particle reconstruction in trigger algorithms , which benefit from faster and more efficient response than previous filters. For those cases, a neural network is trained to reduce background signal, to offer a high-level discriminating variable for a classification problem or to provide a prediction of a certain quantity. These methods can outperform conventional algorithms as the inference is usually performed from multi-dimensional inputs, providing large amounts of information to the learning algorithm. Regarding simulation, the detector simulation is one of the most computational intensive tasks within ATLAS and solutions involving adversarial networks and auto-encoders are being studied to output faster output, specially from the calorimeter simulation. Regarding particle reconstruction and identification, examples of implementations can be found within the τ identification or b-tagging algorithms . In physics analyses, the use of ML is already standarised to typically reconstruct or discriminate the signal process.

5.1 Pipeline

Machine Learning is a very broad umbrella term covering all kinds of algorithms which are not per se optimised for a specific task but are flexible enough to adapt to different problem sets by tuning (training) their parameter set. ML requires besides the model itself also preparation and follow-up processing steps. In which extent they are necessary always depends on the available data, the model and its later application. Figure 7.1 shows such an example workflow (the single steps are explained in more detail in the dedicated sections e.g. sec. 9.2).

Generally, two types of machine learning are distinguished: Supervised learning requiring fully labelled training data and Unsupervised learning not requiring any labelled data. There are also

intermediate approaches called Semi-Supervised learning. In the context of this thesis supervised approaches are used based on Neural Networks (NNs) and Boosted Decision Trees (BDTs). In the following, a statistical parametric (ML) model is denoted as Pmodel(xi; theta) parametrised with the parameters theta while Pdata is the true but unknown distribution. A data set of length N is given as X = (x1, x2, ..., xN), in which each data point i has a feature set xi = (x 1 i , x 2 i , ..., xM i) with M features and true labels yi in case of supervised learning.

t is important to ensure an unbiased training process. For this purpose, at least three orthogonal datasets are needed as indicated in Figure 7.2. The training sample is utilised for the actual algorithm training. The validation set is typically used to choose between different models and to optimise the model further such as hyperparameter optimisation. While for the training itself mostly a loss function is used (see sec. 7.2.3) to find the best parameter set, on the validation set, the performance measures dedicated for the problem set are evaluated (e.g. signal over background ratio) to fine-tune the model choice. The testing sample is only used to evaluate the final performance and is not involved in the training process. In the case of samples with low statistics, one can use cross-validation or also called k-folding [139] where pairs of training and test-/validation sets are partitioned into k subsets.

Typically, in particle physics the event number1 variable is used to split the dataset into the training and testing set. The advantage is that at every point it is clear which events were used for the training 1 The event number is a unique integer number associated to each event not correlated with any physical observable.

5.2 Performance

Even though every ML application is different, the model performance is the decisive measure in the end. Depending on the task, different metrics are used to judge the performance. In the following, the most common approaches are discussed.

Likelihood Discriminant

Loss Function

5.3 Neural networks

Optimiser

Backpropagation

Activation Functions

Regularisation

5.4 BDTs if used

Charged Higgs boson with $H^{\pm} \longrightarrow tb$ search

Neutral scalar produced in $t \longrightarrow qX$ with $X \longrightarrow b\bar{b}$ search

Appendix

Bibliography

Here are the references in citation order.

[1] G. Aad et al. 'Observation of a new particle in the search for the Standard Model Higgs boson with the ATLAS detector at the LHC'. In: *Physics Letters B* 716.1 (2012), 1–29. DOI: 10.1016/j.physletb.2012.08.020 (cited on pages 1, 5).

[2] S. Chatrchyan et al. 'Observation of a new boson at a mass of 125 GeV with the CMS experiment at the LHC'. In: *Physics Letters B* 716.1 (2012), 30–61. DOI: 10.1016/j.physletb.2012.08.021 (cited on pages 1, 5).

[3] LHCb Collaboration. *Test of lepton universality in beauty-quark decays*. 2021. DOI: 10.48550/ARXIV.2103.11769. URL: https://arxiv.org/abs/2103.11769 (cited on pages 1, 30).

[4] B. Abi et al. 'Measurement of the Positive Muon Anomalous Magnetic Moment to 0.46 ppm'. In: *Phys. Rev. Lett.* 126 (14 2021), p. 141801. DOI: 10.1103/PhysRevLett.126.141801 (cited on pages 1, 31).

[5] and M. Aaboud, G. Aad, and B. Abbott. 'Search for charged Higgs bosons decaying into top and bottom quarks at $$ \sqrt{s}=13 $$ TeV with the ATLAS detector'. In: *Journal of High Energy Physics* 2018.11 (2018). DOI: 10.1007/jhep11(2018)085 (cited on page 1).

[6] ATLAS Collaboration. *Search for flavour-changing neutral current interactions of the top quark and the Higgs boson in events with a pair of τ-leptons in pp collisions at $\sqrt{s}$ = 13TeV with the ATLAS detector*. ATLAS-CONF-2022-014. 2022 (cited on page 2).

[7] Armen Tumasyan et al. 'Search for flavor-changing neutral current interactions of the top quark and the Higgs boson decaying to a bottom quark-antiquark pair at $\sqrt{s} = 13$ TeV'. In: *JHEP* 02 (2022), p. 169. DOI: 10.1007/JHEP02(2022)169 (cited on page 2).

[8] Steven Weinberg. 'A Model of Leptons'. In: *Phys. Rev. Lett.* 19 (21 1967), pp. 1264–1266. DOI: 10.1103/PhysRevLett.19.1264 (cited on page 5).

[9] Sheldon L. Glashow. 'Partial-symmetries of weak interactions'. In: *Nuclear Physics* 22.4 (1961), pp. 579–588. DOI: https://doi.org/10.1016/0029-5582(61)90469-2 (cited on page 5).

[10] Abdus Salam. 'Gauge unification of fundamental forces'. In: *Rev. Mod. Phys.* 52 (3 1980), pp. 525–538. DOI: 10.1103/RevModPhys.52.525 (cited on page 5).

[11] S. Abachi et al. 'Search for High Mass Top Quark Production inppCollisions ats=1.8 TeV'. In: *Physical Review Letters* 74.13 (1995), 2422–2426. DOI: 10.1103/physrevlett.74.2422 (cited on pages 5, 28).

[12] 'Observation of Top Quark Production in $\overline{p}p$ Collisions with the Collider Detector at Fermilab'. In: *Phys. Rev. Lett.* 74 (14 1995), pp. 2626–2631. DOI: 10.1103/PhysRevLett.74.2626 (cited on pages 5, 28).

[13] H. Fritzsch, M. Gell-Mann, and H. Leutwyler. 'Advantages of the color octet gluon picture'. In: *Physics Letters B* 47.4 (1973), pp. 365–368. DOI: https://doi.org/10.1016/0370-2693(73)90625-4 (cited on page 5).

[14] Abdus Salam. 'Weak and Electromagnetic Interactions'. In: *Conf. Proc. C* 680519 (1968), pp. 367–377. DOI: 10.1142/9789812795915_0034 (cited on page 5).

[15] W. Pauli. 'Über den Zusammenhang des Abschlusses der Elektronengruppen im Atom mit der Komplexstruktur der Spektren'. In: *Zeitschrift für Physik* 31.1 (1925), pp. 765–783. DOI: 10.1007/BF02980631 (cited on page 6).

[16] P.A. Zyla et al. 'Review of Particle Physics'. In: *PTEP* 2020.8 (2020), p. 083C01. DOI: 10.1093/ptep/ptaa104 (cited on pages 6, 7, 23, 28, 32).

[17] Emmy Noether. 'Invariant variation problems'. In: *Transport Theory and Statistical Physics* 1.3 (1971), pp. 186–207. DOI: 10.1080/00411457108231446 (cited on page 8).

[18] C. N. Yang and R. L. Mills. 'Conservation of Isotopic Spin and Isotopic Gauge Invariance'. In: *Phys. Rev.* 96 (1 1954), pp. 191–195. DOI: 10.1103/PhysRev.96.191 (cited on page 9).

[19] Murray Gell-Mann. 'Symmetries of Baryons and Mesons'. In: *Phys. Rev.* 125 (3 1962), pp. 1067–1084. DOI: 10.1103/PhysRev.125.1067 (cited on page 11).

[20] C. Abel et al. 'Measurement of the Permanent Electric Dipole Moment of the Neutron'. In: *Phys. Rev. Lett.* 124 (8 2020), p. 081803. DOI: 10.1103/PhysRevLett.124.081803 (cited on page 12).

[21] H. David Politzer. 'Reliable Perturbative Results for Strong Interactions?' In: *Phys. Rev. Lett.* 30 (26 1973), pp. 1346–1349. DOI: 10.1103/PhysRevLett.30.1346 (cited on page 12).

[22] David J. Gross and Frank Wilczek. 'Ultraviolet Behavior of Non-Abelian Gauge Theories'. In: *Phys. Rev. Lett.* 30 (26 1973), pp. 1343–1346. DOI: 10.1103/PhysRevLett.30.1343 (cited on page 12).

[23] T. D. Lee and C. N. Yang. 'Question of Parity Conservation in Weak Interactions'. In: *Phys. Rev.* 104 (1 1956), pp. 254–258. DOI: 10.1103/PhysRev.104.254 (cited on page 14).

[24] C. S. Wu et al. 'Experimental Test of Parity Conservation in Beta Decay'. In: *Phys. Rev.* 105 (4 1957), pp. 1413–1415. DOI: 10.1103/PhysRev.105.1413 (cited on page 14).

[25] Peter W. Higgs. 'Broken Symmetries and the Masses of Gauge Bosons'. In: *Phys. Rev. Lett.* 13 (16 1964), pp. 508–509. DOI: 10.1103/PhysRevLett.13.508 (cited on page 18).

[26] P.W. Higgs. 'Broken symmetries, massless particles and gauge fields'. In: *Physics Letters* 12.2 (1964), pp. 132–133. DOI: https://doi.org/10.1016/0031-9163(64)91136-9 (cited on page 18).

[27] F. Englert and R. Brout. 'Broken Symmetry and the Mass of Gauge Vector Mesons'. In: *Phys. Rev. Lett.* 13 (9 1964), pp. 321–323. DOI: 10.1103/PhysRevLett.13.321 (cited on page 18).

[28] Hideki Yukawa. 'On the Interaction of Elementary Particles. I'. In: *Progress of Theoretical Physics Supplement* 1 (Jan. 1955), pp. 1–10. DOI: 10.1143/PTPS.1.1 (cited on page 21).

[29] Nicola Cabibbo. 'Unitary Symmetry and Leptonic Decays'. In: *Phys. Rev. Lett.* 10 (12 1963), pp. 531–533. DOI: 10.1103/PhysRevLett.10.531 (cited on page 23).

[30] Makoto Kobayashi and Toshihide Maskawa. 'CP Violation in the Renormalizable Theory of Weak Interaction'. In: *Prog. Theor. Phys.* 49 (1973), pp. 652–657. DOI: 10.1143/PTP.49.652 (cited on page 23).

[31] Ling-Lie Chau and Wai-Yee Keung. 'Comments on the Parametrization of the Kobayashi-Maskawa Matrix'. In: *Phys. Rev. Lett.* 53 (19 1984), pp. 1802–1805. DOI: 10.1103/PhysRevLett.53.1802 (cited on page 23).

[32] S. L. Glashow, J. Iliopoulos, and L. Maiani. 'Weak Interactions with Lepton-Hadron Symmetry'. In: *Phys. Rev. D* 2 (7 1970), pp. 1285–1292. DOI: 10.1103/PhysRevD.2.1285 (cited on page 24).

[33] *Standard Model Summary Plots June 2021*. Tech. rep. All figures including auxiliary figures are available at https://atlas.web.cern.ch/Atlas/GROUPS/PHYSICS/PUBNOTES/ATL-PHYS-PUB-2021-032. Geneva: CERN, 2021 (cited on page 26).

[34] ATLAS Collaboration. 'A detailed map of Higgs boson interactions by the ATLAS experiment ten years after the discovery'. In: *Nature* 607.7917 (2022), pp. 52–59. DOI: 10.1038/s41586-022-04893-w (cited on page 27).

[35] *Top working group cross-section summary plots June 2022*. Tech. rep. All figures including auxiliary figures are available at https://atlas.web.cern.ch/Atlas/GROUPS/PHYSICS/PUBNOTES/ATL-PHYS-PUB-2022-031. Geneva: CERN, 2022 (cited on page 29).

[36] K. Abe et al. 'Atmospheric neutrino oscillation analysis with external constraints in Super-Kamiokande I-IV'. In: *Physical Review D* 97.7 (2018). DOI: 10.1103/physrevd.97.072001 (cited on page 30).

[37] Lyndon Evans and Philip Bryant. 'LHC Machine'. In: *Journal of Instrumentation* 3.08 (2008), S08001–S08001. DOI: 10.1088/1748-0221/3/08/s08001 (cited on page 33).

[38] 'The ATLAS Experiment at the CERN Large Hadron Collider'. In: *Journal of Instrumentation* 3.08 (2008), S08003–S08003. DOI: 10.1088/1748-0221/3/08/s08003 (cited on page 33).

[39] Esma Mobs. 'The CERN accelerator complex - August 2018. Complexe des accélérateurs du CERN - Août 2018'. In: (2018). General Photo (cited on page 34).

[40] CERN. *Diagram of an LHC dipole magnet. Schéma d'un aimant dipôle du LHC*. 1999. URL: https://cds.cern.ch/record/40524 (cited on page 35).

[41] 'The CMS experiment at the CERN LHC'. In: *Journal of Instrumentation* 3.08 (2008), S08004–S08004. DOI: 10.1088/1748-0221/3/08/s08004 (cited on page 34).

[42] 'The LHCb Detector at the LHC'. In: *Journal of Instrumentation* 3.08 (2008), S08005–S08005. DOI: 10.1088/1748-0221/3/08/s08005 (cited on page 34).

[43] 'The ALICE experiment at the CERN LHC'. In: *Journal of Instrumentation* 3.08 (2008), S08002–S08002. DOI: 10.1088/1748-0221/3/08/s08002 (cited on page 34).

[44] Stephen Myers. *The LEP Collider, from design to approval and commissioning*. John Adams' memorial lecture. Delivered at CERN, 26 Nov 1990. Geneva: CERN, 1991 (cited on page 35).

[45] *Luminosity determination in pp collisions at* $\sqrt{s} = 13$ *TeV using the ATLAS detector at the LHC*. Tech. rep. Geneva: CERN, 2019 (cited on page 36).

[46] *Luminosity Public Results for Run-2*. URL: https://twiki.cern.ch/twiki/bin/view/AtlasPublic/LuminosityPublicResultsRun2 (cited on pages 36, 37).

[47] *Luminosity Public Results for Run-1*. URL: https://twiki.cern.ch/twiki/bin/view/AtlasPublic/LuminosityPublicResults (cited on page 36).

[48] 'The ATLAS Experiment at the CERN Large Hadron Collider'. In: *Journal of Instrumentation* 3.08 (2008), S08003–S08003. DOI: 10.1088/1748-0221/3/08/s08003 (cited on pages 38, 39, 41, 43).

[49] J.J. Goodson. 'Search for Supersymmetry in States with Large Missing Transverse Momentum and Three Leptons including a Z-Boson'. Presented 17 Apr 2012. PhD thesis. Stony Brook University, 2012 (cited on page 44).